

A refined analysis of the low-mass eclipsing binary system T-Cyg1-12664 [★]

Ramón Iglesias-Marzoa^{1,2}, Mercedes López-Morales³, María J. Arévalo^{1,4}, Jeffrey L. Coughlin⁵, and Carlos Lázaro^{1,4}

¹ Astrophysics Department, Universidad de La Laguna, E-38205 La Laguna, Tenerife, Spain

² Centro de Estudios de Física del Cosmos de Aragón, Plaza San Juan 1, E-44001, Teruel, Spain
e-mail: riglesias@cefca.es

³ Harvard-Smithsonian Center for Astrophysics, 60 Garden Street, Cambridge, MA 02138, USA

⁴ Instituto de Astrofísica de Canarias, E-38200, La Laguna, Tenerife, Spain

⁵ SETI Institute, 189 Bernardo Ave, Mountain View, CA 94043, USA

Received September 15, 1996; accepted March 16, 1997

ABSTRACT

Context. The observational mass-radius relation of main sequence stars with masses between ~ 0.3 and $1.0 M_{\odot}$ reveals deviations between the stellar radii predicted by models and the observed radii of stars in detached binaries.

Aims. We generate an accurate physical model of the low-mass eclipsing binary T-Cyg1-12664 in the Kepler mission field to measure the physical parameters of its components and to compare them with the prediction of theoretical stellar evolution models.

Methods. We analyze the Kepler mission light curve of T-Cyg1-12664 to accurately measure the times and phases of the primary and secondary eclipse. In addition, we measure the rotational period of the primary component by analyzing the out-of-eclipse oscillations that are due to spots. We accurately constrain the effective temperature of the system using ground-based absolute photometry in B, V, R_C , and I_C . We also obtain and analyze $VR_C I_C$ differential light curves to measure the eccentricity and the orbital inclination of the system, and a precise T_{eff} ratio. From the joint analysis of new radial velocities and those in the literature we measure the individual masses of the stars. Finally, we use the PHOEBE code to generate a physical model of the system.

Results. T-Cyg1-12664 is a low eccentricity system, located $d=360\pm 22$ pc away from us, with an orbital period of $P = 4.1287955(4)$ days, and an orbital inclination $i=86.969\pm 0.056$ degrees. It is composed of two very different stars with an active G6 primary with $T_{\text{eff}1}=5560\pm 160$ K, $M_1=0.680\pm 0.045 M_{\odot}$, $R_1=0.799\pm 0.017 R_{\odot}$, and a M3V secondary star with $T_{\text{eff}2}=3460\pm 210$ K, $M_2=0.376\pm 0.017 M_{\odot}$, and $R_2=0.3475\pm 0.0081 R_{\odot}$.

Conclusions. The primary star is an oversized and spotted active star, hotter than the stars in its mass range. The secondary is a cool star near the mass boundary for fully convective stars ($M \sim 0.35 M_{\odot}$), whose parameters appear to be in agreement with low-mass stellar model.

Key words. Stars: fundamental parameters – Stars: low-mass – Binaries: eclipsing – Binaries: spectroscopic

1. Introduction

T-Cyg1-12664 (KIC 10935310, 2MASS J19513982+4819553) is a low-mass detached eclipsing binary (LMDEB) at $\alpha=19:51:39.824$, $\delta=+48:19:55.38$ (J2000.0). It was first discovered in the T-Cyg1 field of the Trans-Atlantic Exoplanet Survey (TrES; Alonso et al. 2004), and it is also in the Kepler mission field of view. Because of its intermediate orbital period (~ 4.129 d) and low mass ratio ($q \approx 0.55$), this system can serve as a benchmark for low-mass ($M < 1 M_{\odot}$) stellar evolution models that have problems with the radii predicted for the stars.

The discovery and first analysis of T-Cyg1-12664 was reported by Devor et al. (2008a) and Devor (2008) using TrES photometric data. They obtained a small number of radial velocity (RV) observations, including only one RV measurement of the faint secondary star. Their RV measurements show that the period initially identified in the TrES photometry (8.26 days) was in fact of 4.129 days, and a secondary eclipse would be buried in the TrES data. From that first analysis Devor (2008)

estimate masses of about $0.62 M_{\odot}$ and $0.32 M_{\odot}$ for the primary and secondary. Çakırlı et al. (2013) reanalyzed this system using new RV measurements, the high precision Kepler mission light curves and R-band ground-based photometry and obtained the following values for the masses and radii of the stars: $M_1 = 0.680\pm 0.021 M_{\odot}$, $R_1 = 0.613\pm 0.007 R_{\odot}$; and $M_2 = 0.341\pm 0.012 M_{\odot}$, $R_2 = 0.897\pm 0.012 R_{\odot}$. In their study, while the radius of the primary is consistent with main sequence low-mass stellar models, the radius of the secondary defies interpretation as a main-sequence star.

After its publication in Devor et al. (2008a), we included T-Cyg1-12664 in our observing program to refine the physical parameters of several LMDEBs. Here we present a thorough analysis of the system based on the Kepler photometry, new ground-based multiband photometry and RV measurements, and a specific photometric calibration carried out to obtain unbiased colors and precise, photometry-based effective temperatures. The outline of this work is as follows. In Sects. 2 and 3 we describe the Kepler and the ground-based RV and photometric observations. Section 4 describes a careful analysis of the system, including specific sections for a consistent photometric calibration, effective temperature, a careful treatment of the third light, and

[★] Tables 1, 2, 3 and 10 are only available in electronic form at the CDS via anonymous ftp to cdsarc.u-strasbg.fr (130.79.128.5) or via <http://cdsweb.u-strasbg.fr/cgi-bin/qcat?J/A+A/>

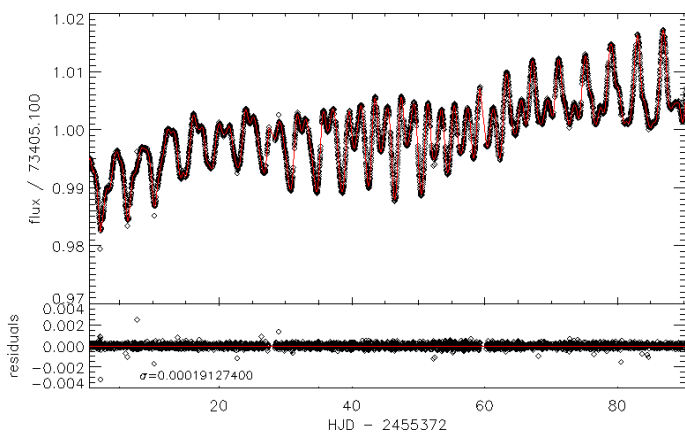


Fig. 1. Fit of an order 300 Legendre polynomial to the Kepler data in quarter 6. The upper panel shows the out-of-eclipse light curve and the fit (red line). The lower panel shows the residuals of the fit.

the orbital eccentricity. Finally, the absolute parameters and the distance of the system are computed in Sect. 6, with Sect. 6.3 devoted to comparing our results to the stellar models and previous results.

2. Light-curve observations

2.1. Kepler observations

T-Cyg1-12664 was observed by the Kepler spacecraft in Long Cadence mode from Q0 through Q17 (JD 2454953.54 – JD 2456424.00). The observations were reduced using the Kepler mission pre-search data conditioning (PDC) pipeline (Jenkins et al. 2010), which produces high quality light curves like the ones illustrated in Figs. 1 and 2 for Q6. The instrumental systematics and spot-related activity in this star are readily visible in the Kepler light curves with out-of-eclipse variations deeper than the secondary eclipse.

We detrended the light curves from each quarter following a procedure similar to Slawson et al. (2011), by fitting Legendre polynomials to the out-of-eclipse data. The result for one quarter (Q6) is shown in Fig. 2. For T-Cyg1-12664 we had ephemeris information from preliminary works, so we could exclude the time intervals affected by eclipses, and it was not necessary to apply the iterative processes described in Slawson et al. (2011). Because of the effects of the spacecraft safe-modes and triggers, some quarters were divided in smaller intervals, but this detrending process was applied to all the Kepler mission photometry encompassing an interval of 1470 days. Typical Legendre polynomials orders were between 30 and 300, depending on the complexity of the variations and duration of the light-curves intervals. The result of this detrending is illustrated in the bottom panel of Fig. 2. This detrended light curve, provided in Table 1, was subsequently analyzed together with the ground-based photometry described in Sect. 2.2.

We note that this detrending process has the disadvantage of potentially removing information from the light curve, such as heating effects and proximity effects that are due to the shape of the stars. However, as we demonstrate in subsequent sections, these effects are negligible in T-Cyg1-12664, because of the large separation between the stars.

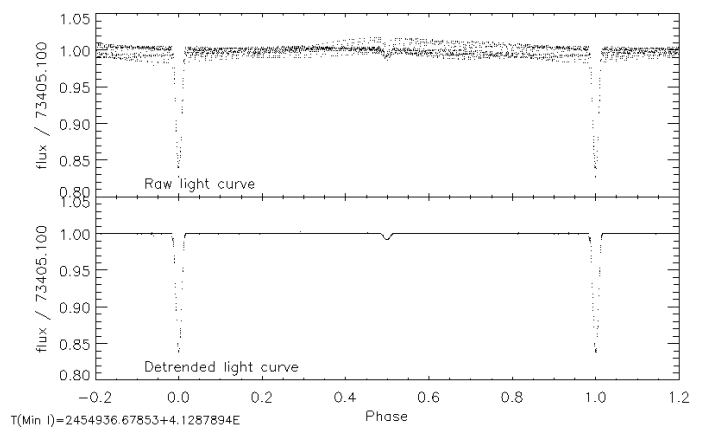


Fig. 2. Effect of the detrending over the phased light curve of Q6 quarter. Upper panel shows the raw light curve and lower panel shows the light curve after applying the Legendre polynomial fitted in Fig. 1.

2.2. Ground-based observations

We observed T-Cyg1-12664 with the CAMELOT camera at the IAC80 telescope in Tenerife, Spain, in VR_CI_C bands, over 14 nights, between 2009-04-04 and 2010-10-01 UT (JD 2454936.6 – JD 2455471.5), when eclipses occurred. We also requested a routinary observation program at the same telescope to sample out-of-eclipse phases. CAMELOT is equipped with a back-illuminated E2V 2048x2048 sensor with squared $13.5 \mu\text{m}$ pixels, which results in a plate scale of $0.''304/\text{pix}$ and a $10.''4 \times 10.''4$ field of view.

Although CAMELOT has two readout channels, all the observations were made using one channel to avoid systematic effects between the object and the comparison stars. Exposure times ranged from 100 s to 180 s in V band, 65 s to 95 s in R_C band, and 60 s to 90 s in I_C band, depending on the seeing and the atmospheric transparency. Each night, we monitored T-Cyg1-12664 continuously over an altitude limit of 30 degrees (airmass ≤ 2) above the horizon. We also acquired bias frames and dome flats in all the filters at the beginning of each night.

We used standard reduction techniques, including bias subtraction, flat-field correction, and alignment of all images to a common reference system, to process the frames. We analyzed the corrected frames using the phot aperture photometry package in IRAF and a custom differential photometry pipeline designed to deal with large sets of frames. The pipeline first performs aperture photometry for a set of preselected comparison stars and the target, for a range of aperture sizes. Using the flux within each aperture, the pipeline computes the signal-to-noise ratio (S/N) of the target using the CCD equation (Merline & Howell 1995, eq. 25), and selects the aperture radius that produces the maximum S/N. This aperture is then used to extract the flux of all the stars in that frame. This procedure accounts for seeing and transparency variations along the night. The CCD equation was also used to compute the formal errors in the photometry. We imposed a limit of 9 pixels to the maximum aperture radius to avoid contamination by nearby stars as is the case for T-Cyg1-12664 (see Sect. 4.5). The selected comparison stars proved to be stable during all the observing runs. We generated V , R_C , and I_C differential light curves of the target dividing its flux by the combined flux of all the comparison stars. Owing to the small field of view of the telescope no differential extinction effects were taken into account. Our VR_CI_C photometry (given in Table 2) includes seven primary and four secondary eclipses which, when added to those from the Kepler,

Çakırlı et al. (2013) and TrES photometry, enable us to improve the period of the system and search for period variations.

3. Radial velocity observations

We observed T-Cyg1-12664 as part of a larger program to produce accurate radial velocity curves of low-mass binaries (see Coughlin 2012). We collected radial velocity observations over two seasons (June – December 2010 and May – September 2011), with the Dual Imaging Spectrograph (DIS) on the 3.5-m at Apache Point Observatory and the R-C Spectrograph on the 4-m at Kitt Peak National Observatory (KPNO). With DIS we observed using its red channel with the R1200 grating, which gives a resolution of 0.58 \AA per pixel, or $R \approx 10,000$. The wavelength range was set to $\sim 5900 - 7100 \text{ \AA}$ for the first observing season, and $\sim 5700 - 6800 \text{ \AA}$ for the second. For the R-C Spectrograph, we used the KPC-24 grating in second order, resulting in a resolution of 0.53 \AA per pixel, or $R \approx 10,000$, with the wavelength range set to $\sim 5700 - 6750 \text{ \AA}$. We collected a total of 31 individual spectra for T-Cyg1-12664, in addition to bias, dark, and flatfield calibration frames. We also collected HeNeAr lamp frames before or after each target observation to use as wavelength calibrations.

All raw frames were bias, dark, and flat-field corrected. For the DIS observations, column 1023 is a dead column, and thus we replaced those values by a linear interpolation between the two neighboring columns. We also removed cosmic rays from all frames using a Laplacian edge algorithm implemented in the `lacos_spec` IRAF package (see van Dokkum 2001). Finally, we extracted one-dimensional spectra from each image, including sky background subtraction, using the IRAF package `apall`. After wavelength calibration, all science spectra were flattened and normalized by fitting a 20-piece cubic spline fit over ten iterations, during which points 3σ above the fit or 1.5σ below the fit were rejected. For each spectrum, we calculated the barycentric Julian date in terrestrial time, BJD(TT), and corrected them to the reference frame of the solar system barycenter using the IRAF task `bcvcorr`.

For all binaries we attempted to extract the radial velocity of each star in each frame, $V_{1,j}$ and $V_{2,j}$, where 1 and 2 denote the primary and secondary stars, and j is the frame number, using a new exploratory method: instead of using cross-correlations, we directly fit reference spectra to each observed spectrum via a traditional standard deviation minimization, which is equivalent to minimizing χ^2 , assuming all observed points have equal errors. Specifically, for each observed spectrum, we fit for the velocity of each reference spectra, as well as for their luminosity ratio, $\alpha = L_1/L_2$, for a total of three free parameters. During the fitting, the original observed spectrum is never changed, and thus it can have any arbitrary number and distribution of wavelength and flux value pairs. Given a total of M observed spectra, each with N_j points, taken at times t_j , we want to find the values of $V_{1,j}$, $V_{2,j}$, and α at each t_j , that minimize the function

$$\sum_{j=1}^M \sum_{i=1}^{N_j} \left(F_{0,i} - \frac{\alpha \cdot F_1 \left(\lambda_{0,i} \cdot \left(1 - \frac{V_{1,j}}{c} \right) \right) + F_2 \left(\lambda_{0,i} \cdot \left(1 - \frac{V_{2,j}}{c} \right) \right)}{\alpha + 1} \right)^2, \quad (1)$$

where $F_{0,i}$ is the flux of an observed spectrum at a given wavelength, $\lambda_{0,i}$, $F_1(\lambda)$, and $F_2(\lambda)$ are the fluxes of reference stars 1 and 2 at a given wavelength, and c is the speed of light. We

determine $F_1(\lambda)$ and $F_2(\lambda)$ by cubic splines interpolation of the original reference spectra.

For reference spectra, we used the normalized (flattened) synthetic spectra from Munari et al. (2005). The Munari et al. (2005) grid we used covers models with $3500 \geq T_{\text{eff}} \geq 10,000$ in steps of 250 K, $0.0 \geq \log g \geq 5.0$ in steps of 0.5 dex, $-2.5 \geq [M/H] \geq 0.5$ in steps of 0.5 dex, and $0 \geq V_{\text{rot}} \geq 100 \text{ km/s}$ in steps of 10 km/s. To ensure that we found the global minimum in both selected reference spectra and their velocities, we performed a global grid search looping over all possible combinations of α , $V_{1,j}$, $V_{2,j}$, T_1 , T_2 , using a common $[M/H]$ for both reference spectra, and $\log g$ and V_{rot} for each reference star. We compared the radial velocities found by this method with those obtained using the well-tested TODCOR code (Zucker & Mazeh 1994), and find consistent results for all the binaries in our program.

The errors in the derived radial velocities were computed using a bootstrapping re-sampling method iterated over 10000 times. The adopted errors correspond to the 1σ confidence interval of the distribution of bootstrapping solutions. To estimate the errors in the derived temperatures, we used the spectroscopic quality-of-fit parameter (López-Morales & Bonanos 2008; Behr 2003), defined as

$$z = \sqrt{N} \left(\frac{rms^2}{rms_{min}^2} - 1 \right), \quad (2)$$

where N is the number of data points, rms^2 is the standard deviation of the fit under consideration, and rms_{min}^2 is the best fit found. The z parameter is similar to a reduced χ^2 in the absence of known errors on the individual points. By definition $z = 0$ at the best-fit, and the 1σ confidence interval corresponds to $z = 1$.

In the particular case of T-Cyg1-12664, the spectrum of the secondary is too weak, and we were unable to detect any significant radial velocity measurements for the secondary star over any reasonable parameter ranges. Thus, we treated the system as a single-lined binary by fixing the value of α to 9 999 and only fitting for the parameters of the primary star $V_{1,j}$, T_{eff} , $[M/H]$, $\log g$ and V_{rot} . The resultant radial velocities are listed in Table 3. In addition, the best fit of the primary's spectra to the grid of synthetic spectra gives a $T_{\text{eff}} = 5750 \pm 250 \text{ K}$, $\log g = 4.5 \pm 0.5$, $[M/H] = -0.5 \pm 0.5$ and $v_r \sin i = 40 \pm 10 \text{ km s}^{-1}$. This T_{eff} is in agreement with the one obtained in Sect. 4.2 using photometric colors. The metallicity appears to be lower than the typical for stars near the Galactic plane (see Section 6.2), which would have near-solar metallicity. We attribute this result to the rather coarse sampling in metallicity of our models, and therefore adopt solar metallicity for this system in the remaining analysis.

We note that, although this χ^2 minimization technique yields values of the radial velocities and other stellar parameters consistent with those obtained via other methods in the case of T-Cyg1-12664, the technique can be prone to systematics introduced by the presence of correlated noise or not well modeled spectral instrumental profiles, especially in the case of low S/N spectra. It is therefore advisable to have results checked against other methods like TODCOR.

4. Analysis of the system

4.1. Photometric calibration and colors

In Table 4, we compile all the available photometry for T-Cyg1-12664 in public catalogs. We found inconsistencies between some of the passband magnitudes reported by different catalogs, e.g. the B and V magnitudes reported by the GSC and NOMAD

Table 4. Photometry in several bands for T-Cyg1-12664 obtained from photometric catalogs.

Bandpass	Magnitude	Source
<i>V</i>	13.520±0.190	GSC ^a
<i>B</i>	14.040±0.416	GSC2.3.2 ^a
<i>V</i>	13.108±0.297	GSC2.3.2 ^a
<i>B</i>	13.530	NOMAD ^{b,c}
<i>V</i>	13.120	NOMAD ^{b,c}
<i>R</i>	13.500	NOMAD ^b
<i>B1</i>	14.460	USNO-B1 ^d
<i>B2</i>	14.020	USNO-B1 ^d
<i>R1</i>	13.130	USNO-B1 ^d
<i>R2</i>	13.500	USNO-B1 ^d
<i>I2</i>	13.210	USNO-B1 ^d
<i>r</i>	12.400	USNO-A2 ^e
<i>b</i>	13.100	USNO-A2 ^e
<i>B</i>	13.530	UCAC3 ^{e,f}
<i>R2</i>	12.512	UCAC3 ^{e,f}
<i>I</i>	11.858	UCAC3 ^{e,f}
<i>U</i>	13.905±0.021	Everett et al. (2012)
<i>B</i>	13.864±0.024	Everett et al. (2012)
<i>V</i>	13.280±0.018	Everett et al. (2012)
<i>g'</i>	13.541	Sloan Digital Sky Survey
<i>r'</i>	13.052	Sloan Digital Sky Survey
<i>i'</i>	12.911	Sloan Digital Sky Survey
<i>z'</i>	12.843	Sloan Digital Sky Survey
<i>D51</i>	13.327	Kepler mission ^g
<i>Kepler</i>	13.100	Kepler mission
<i>J</i>	11.911±0.024	2MASS ^h
<i>H</i>	11.582±0.015	2MASS ^h
<i>K_s</i>	11.529±0.021	2MASS ^h

Notes.
^(a) Identifier: GSC 0356101711.

^(b) Identifier: 1383-0349082.

^(c) Mag from YB2.

^(d) Identifier: 1383-0345184.

^(e) Identifier: U1350 11189502.

^(f) Mag from SuperCosmos.

^(g) Band centered in 510 nm, see Brown et al. (2011).

^(h) Identifier: 2MASS J19513982+4819553.

catalogs disagree by 0.4–0.5 mags. The differences are too large to be explained by stellar activity, or even accounting for the depth of the eclipses (~0.20 in the Kepler band). We do not have an explanation for these discrepancies but, concerned about introducing large errors in the determination of parameters for this system, we proceeded to derive new, consistent colors.

We performed photometric calibrations of several objects, including T-Cyg1-12664, over two photometric nights in July and August 2012, during out-of-eclipse phases. We used the Trömsø CCD Photometer in full frame mode (TCP, Östensen 2000; Östensen & Solheim 2000), at the IAC80 telescope (CAMELOT was not available at the time of these observations). The TCP is built around a Texas Instruments 1024x1024 CCD sensor and produces a 9.6 field of view, with a plate scale of 0.537 pixel⁻¹, at the IAC80's focal plane.

We observed several Landolt standard fields (Landolt 2009), covering objects with a wide range of colors and airmasses, and using Johnson-Cousins *B*, *V*, *R_C*, and *I_C* filters. A log of the observations is shown in Table 5. We measured the flux of the standard stars via standard aperture photometry, using the IRAF

Table 5. Observed Landolt fields. The number of measurements is the global count for different air masses.

Night	Field	N _{stars}	N _{meas}	Airmass range
2012-07-26	SA110SF3	8	19	1.130-2.519
	PG1633+099	8	9 ^a	1.055-2.590
2012-08-18	SA110SF3	8	4 ^b	1.158-2.435
	PG0231+051	6	9 ^c	1.086-1.690
	PG1657+078	6	6	1.076 - 2.542

^(a) 8 measurements for the *B* and *V* filters. ^(b) 6 measurements for the *I_C* filter. ^(c) 10 measurements for the *V* filter.

Table 6. Standard transformation coefficients from Eq. 3 for the two nights. The uncertainties are shown in parentheses affecting the last two digits.

Parameter	2012-07-26	2012-08-18
<i>b</i> ₀	2.7185(30)	2.7947(65)
<i>b</i> ₁	0.2262(18)	0.2250(38)
<i>b</i> ₂	0.0101(39)	0.0430(90)
<i>b</i> ₃	-0.0204(22)	-0.0342(49)
<i>b</i> ₄	-0.0038(13)	-0.0186(27)
<i>v</i> ₀	2.7752(25)	2.8607(44)
<i>v</i> ₁	0.1184(13)	0.1170(24)
<i>v</i> ₂	0.0436(30)	0.0575(56)
<i>v</i> ₃	0.0025(13)	-0.0082(27)
<i>v</i> ₄	0.01621(82)	0.0163(15)
<i>r</i> ₀	2.8779(29)	2.9391(46)
<i>r</i> ₁	0.0877(13)	0.0905(24)
<i>r</i> ₂	-0.0662(61)	0.029(11)
<i>r</i> ₃	-0.0096(21)	-0.0208(40)
<i>r</i> ₄	0.0940(29)	0.0501(56)
<i>i</i> ₀	3.2383(37)	3.3249(52)
<i>i</i> ₁	0.0426(17)	0.0482(29)
<i>i</i> ₂	-0.2608(78)	-0.209(12)
<i>i</i> ₃	0.0024(26)	-0.0326(45)
<i>i</i> ₄	0.0717(39)	0.0865(73)

package `apphot`, and adopting an aperture of 14'' (a 13 pixel radius in the TCP images), to match the Landolt aperture widths.

The extinction correction and transformation to the standard photometric system was performed simultaneously solving the set of equations

$$\begin{aligned}
m_B &= B + b_0 + b_1 X_B + b_2 (B - V) + b_3 X_B (B - V) + b_4 (B - V)^2 \\
m_V &= V + v_0 + v_1 X_V + v_2 (B - V) + v_3 X_V (B - V) + v_4 (B - V)^2 \\
m_{R_C} &= R_C + r_0 + r_1 X_{R_C} + r_2 (V - R_C) + r_3 X_{R_C} (V - R_C) + r_4 (V - R_C)^2 \\
m_{I_C} &= I_C + i_0 + i_1 X_{I_C} + i_2 (V - R_C) + i_3 X_{I_C} (V - R_C) + i_4 (V - R_C)^2
\end{aligned} \tag{3}$$

where the instrumental magnitudes appear on the left-hand side of the equations, the absolute magnitudes are denoted as *B*, *V*, *R_C*, and *I_C*, and the airmass values as *X*. The equations were solved using least-square techniques, and the resulting coefficients for each night are summarized in Table 6. The absolute magnitudes obtained for T-Cyg1-12664 as the average of the results for each night are summarized in Table 7. In that same table, we also list color indexes, including the near-infrared *JHK_S* bands from 2MASS (Skrutskie et al. 2006).

Our *B* and *V* calibrated magnitudes are slightly fainter than the ones from Everett et al. (2012). We attribute the small differences ($\Delta B=0.073$, $\Delta V=0.019$), to stellar activity variations, as seen in Fig. 2. In the Kepler light curve these variations are

Table 7. Calibrated magnitudes and color indices for T-Cyg1 obtained from our photometric calibration. The infrared magnitudes are taken from 2MASS (see Table 4).

Band	Adopted value (mag)
B	13.937 ± 0.002
V	13.299 ± 0.005
R_C	12.925 ± 0.005
I_C	12.511 ± 0.004
$B - V$	0.638 ± 0.005
$V - R_C$	0.374 ± 0.007
$V - I_C$	0.788 ± 0.006
$V - K_S$	1.770 ± 0.022
$R_C - I_C$	0.414 ± 0.006
$I_C - K_S$	0.982 ± 0.021
$J - H$	0.329 ± 0.028
$J - K_S$	0.382 ± 0.032
$H - K_S$	0.053 ± 0.026

of $\Delta m_{Kp} \sim 0.022$, which is very close to the variation we see in V band. The $B - V$ index obtained by Everett et al. (2012) is 0.584 ± 0.030 , which is slightly bluer than ours, mainly as a consequence of the difference in the B measurements.

4.2. Effective temperature

We derived the effective temperature of the system, T_{eff} , using the empirical and model dependent, temperature–color relations listed in Table 8, our BVR_CI_C colors derived in Sect. 4.1, and the colors of the system published in 2MASS (Skrutskie et al. 2006), and the SDSS (Eisenstein et al. 2011). All those colors were measured outside of eclipses, which guarantees that no systematics were introduced by the dimming of the system during eclipse events. We still have the effect of stellar variability, which results in small variations of the color indexes. Those variations are accounted for in the T_{eff} errors reported in Table 8.

Table 8 summarizes the values of the T_{eff} derived using each temperature–color relation. We assumed negligible reddening in the direction of T-Cyg1-12664 when computing the colors but, in any case, the effect of the reddening over the distances involved will be smaller than the uncertainties in colors among the optical and IR bands, as a consequence of those colors being measured in different epochs and the intrinsic photometric variability of the system. The mean effective temperature adopted for the system, computed as the average of all the results in Table 8, is 5560 ± 160 K. This value is within 1σ of the value of T_{eff} obtained from fitting our spectra in Sect. 3, and corresponds to a spectral type $G6V$, based on the tabulated values of Mamajek (2015). We adopted this result as the spectral type for the primary.

Our T_{eff} and spectral type of the primary do not agree with those derived by Devor (2008) and Çakırlı et al. (2013). In those studies the authors claim a $K5V$ spectral type for the system and a mean $T_{\text{eff}} = 4320 \pm 100$ K. The main difference between their calculations and ours is their use of B and V magnitudes from the USNO catalog and GSC2.3.2, which we noticed in Sect. 4.1, are unreliable.

4.3. Spectral energy distribution

Given the difference between the spectral type obtained in this work and those in the literature, and as an additional check to the absolute photometry values derived in Sect. 4.1, we com-

Table 8. Mean effective temperature estimations resulting from our photometric calibration, 2MASS and SDSS photometry and our spectroscopy for T-Cyg1-12664. The interstellar reddening was not taken into account for this computation.

Calibrations	Color indices	T_{eff} (K)
Empirical		
Cox (2000)	$(B - V), (R - I_C)$	5490 ± 350
Cox (2000) ^a	$(V - K_S), (J - H)$	5610 ± 200
Arribas & Martinez Roger (1988)	$(V - K_S)$	5260 ± 60
Ballesteros (2012)	$(B - V)$	5820 ± 19
Masana et al. (2006)	$(V - K_S)$	5460 ± 15^b
Ivezić et al. (2008)	$(g' - r')$	5527 ± 44
Fukugita et al. (2011)	$(g' - r')$	5564 ± 28
Model dependent		
Bessell (1979)	$(B - V), (V - I_C), (R_C - I_C)$	5420 ± 300
Houdashelt et al. (2000)	$(B - V), (V - R_C), (V - I_C), (V - K_S), (J - K_S), (H - K_S)$	5680 ± 230
Lejeune et al. (1998)	$(B - V), (V - I_C), (V - K_S), (R_C - I_C), (J - H), (J - K_S), (H - K_S)$	5570 ± 290
This work	Spectroscopy	5750 ± 250
Mean value (adopted)		5560 ± 160

Notes.

(^a) Interpolation from Table 7.6. (^b) For $\log g = 4.5$, $[M/H] = -0.5$.

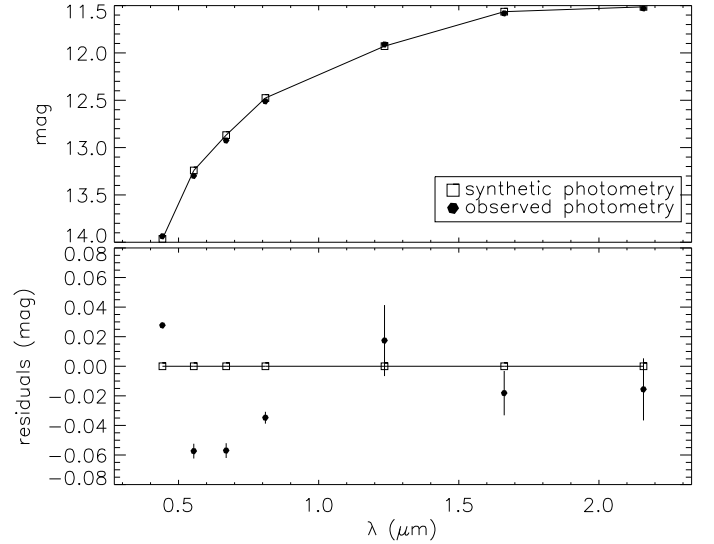


Fig. 3. Comparison between the absolute optical and 2MASS photometry with the synthetic photometry obtained for a Kurucz model with $T_{\text{eff}} = 5500$ K, $\log g = 4.5$, and $[M/H] = -0.5$. The uncertainties in the upper panel are smaller than the point sizes.

pared the optical and near-infrared colors measured for T-Cyg1-12664 to a Kurucz (1993) model template with $T_{\text{eff}} = 5500$ K, $\log g = 4.5$, and $[M/H] = -0.5$. The result is shown in Fig. 3, where the fit between the model and the observations produces an rms of 0.037 mags. We also repeated the same comparison with the calibrated photometry in Table 7 and a template model with the same metallicity and $\log g$, but with $T_{\text{eff}} = 4250$ K from Çakırlı et al. (2013). The best fit in this case produces an rms of 1.029 mags, with a clear systematic trend. Based on these results we conclude that the value of 5560 ± 160 K is a good estimate of the actual T_{eff} for T-Cyg1-12664.

4.4. Rotation and synchronicity parameter

The Kepler raw light curves of the system (see, for example, Fig. 2) reveals periodic photometric variations owing to spots, and with a period clearly different from that of the binary. In addition, and given the large differences in luminosity between

the primary and secondary stars, we can attribute those photometric variations to spots on the primary star. Therefore, we can measure the rotation period of the primary, assuming that the spots rotate jointly with the photosphere. After normalizing each quarter of the Kepler raw light-curve, and removing the eclipses using the ephemeris equation of the system (see Sect. 4.6), we calculated Lomb-Scargle periodograms (Scargle 1982) for each normalized light curve. A prominent peak is seen in the periodogram from which we obtained rotation periods in a range between 3.840778 d and 4.250872 d. We attribute those variations to changes in the different spot configurations over the time span of the observations, and adopted a mean rotation period of $P_{rot} = 3.968 \pm 0.091$ d. That rotation period results in a synchronicity parameter $F = \omega_{rot}/\omega_{orb} = 1.041 \pm 0.024$, using the period of the binary computed in Sect. 4.6. This value of F is too small to produce a significant deviation in the computed stellar radius and lets us assume that the primary star is rotationally synchronized with the orbital period. This P_{rot} must be taken as an estimate, given that the star is not a rigid body with a well defined rotation period and, thus, this period depends on the latitude of the spots. For each of the two main spots in the Q6 interval, we measured the times t_{min} of each associated minima and plotted the difference $T_0 - t_{min}$ versus the sequential number of each minima, with T_0 defined as the time of a primary eclipse. We fit a straight line to each spot's dataset and obtained slopes of 3.9659 ± 0.0092 d and 3.988 ± 0.010 d, which confirms the presence of differential rotation, as already revealed by the observed range of rotational periods. In addition, the spot with the lower rotation period is the one with lower latitude in the Q6-1 epoch (see Sect. 5.5), which suggests that the primary has solar-type differential rotation (see, for example, Reinhold & Arlt 2015; Lanza et al. 2014, and references therein).

4.5. Third light

T-Cyg1-12664 has an optical companion at a distance of 4.''6 as pointed by Çakırlı et al. (2013), which is clearly seen in our images. We call this contaminant star T-Cyg1-C in the rest of the text. The aperture of our ground-based photometry avoids contamination by light from this star. Thus, our $VR_C I_C$ differential photometry is free of this third light contribution. However, Kepler uses a photometric aperture of $\sim 10 - 11$ pix for T-Cyg1-12664 (roughly 3×3 pix), depending on the season, with a plate scale of $3.''98/\text{pix}$. Given that this contaminant is not listed in the Kepler Input Catalog (KIC) it wouldn't have been accounted for during Kepler's third light calibration, and the Kepler light curve of T-Cyg1-12664 is affected by the flux of T-Cyg1-C.

To estimate the amount of third light in the Kepler passband, we had to rely on the flux of the contaminant in V , R_C , and I_C . We applied the photometric calibration performed on the night of 2012-07-26 to T-Cyg1-C, to obtain its magnitudes and colors listed in Table 9. From those colors we adopted $T_{\text{eff}} = 3761 \pm 56$ K for T-Cyg1-C, based on the calibrations of Cox (2000), Bessell (1991, 1979) and Lejeune et al. (1998). We didn't use the $B - V$ color index since their T_{eff} is not consistent with the results of the other color indices and the B -band magnitude is too faint. Thus, we rely only on the colors that make use of V , R_C , and I_C photometry. From the obtained T_{eff} , and assuming it is a main-sequence star, we adopted a spectral type of M0V for this star, using the tables in Mamajek (2015).

To estimate the Kepler band flux, K_p , for T-Cyg1-C we fit a spectral energy distribution (SED) using the observed colors and a Kurucz model spectrum with $T_{\text{eff}}=3750$ K and solar metallicity and obtain a geometric dilution parameter of

Table 9. Fluxes and colors for T-Cyg1-C, the contaminant in the Kepler passband.

Parameter	Value
B	18.600 \pm 0.039
V	17.822 \pm 0.029
R	16.975 \pm 0.020
I	16.009 \pm 0.017
$B - V$	0.778 \pm 0.049
$V - R_C$	0.847 \pm 0.035
$V_C - I_C$	1.813 \pm 0.034
$R_C - I_C$	0.966 \pm 0.026

Notes. The color index B-V is not used in the computation of the T_{eff} of the contaminating star (see text).

$(R_*/D)^2 = (5.65 \pm 0.14) \times 10^{-22}$ over the integrated $VR_C I_C$ bands (see Moro & Munari 2000). The uncertainty was computed performing Monte-Carlo fits over 100 iterations. We used the same Kurucz spectrum used in the synthetic SED, scaled by the computed dilution factor and integrated over the Kepler response function¹ to estimate the contaminant flux due to T-Cyg1-C. The uncertainty was also computed with a Monte-Carlo analysis, as in the dilution factor case, and the obtained value is $F^{K_p} = (5.88 \pm 0.15) \times 10^{-9}$ erg cm⁻² s⁻¹. For T-Cyg1-12664 we followed the same procedure but using a dilution factor of $(R/D)^2 = (2.7291 \pm 0.0082) \times 10^{-21}$, which results in a Kepler flux of $F_K = (2.5006 \pm 0.0071) \times 10^{-7}$ erg cm⁻² s⁻¹.

Using these fluxes for the binary and the contaminant, the third light ratio in the Kepler band results in

$$l_3^{K_p} = 0.02297 \pm 0.00058.$$

As a check of the feasibility of this result, we compared this value with the estimated amount of third light in the V , R_C , and I_C bands using images taken the night of 2010-08-28 at an orbital phase of 0.285. The values obtained for the differences in magnitude between T-Cyg1-12664 and T-Cyg1-C were $\Delta V = 4.619 \pm 0.028$, $\Delta R_C = 4.186 \pm 0.018$, and $\Delta I_C = 3.463 \pm 0.013$, which translate into third light ratios at each passband

$$l_3^V = 0.0140 \pm 0.0004; l_3^{R_C} = 0.0207 \pm 0.0003; \\ l_3^{I_C} = 0.0396 \pm 0.0005.$$

These results are of the same order of magnitude as those obtained for the K_p band. No other nearby stars are observed in the IAC80 images and there are no signs of apsidal motion in the eclipse timings (primary or secondary) in the time span of the observations (see Sect. 4.6). Thus, we assumed that there is no other significant source of third light in the system and we adopted the value for the Kepler band as the only source. Nonetheless, during the modelling of this system in Sect. 5.5 we ran tests to ensure that no other source of third light affects the $BVR_C I_C$ bands, for example, if T-Cyg1-12664 were a multiple system with a third object that is not resolved in our images. All these tests yielded negative results.

4.6. Orbital period analysis and ephemeris

We calculated the central times of eclipse in both the Kepler detrended light curves and the IAC80 light curves. To find the central times of eclipse in the Kepler light curve, we fit either third

¹ Available at <http://keplergergo.arc.nasa.gov/CalibrationResponse.sh>

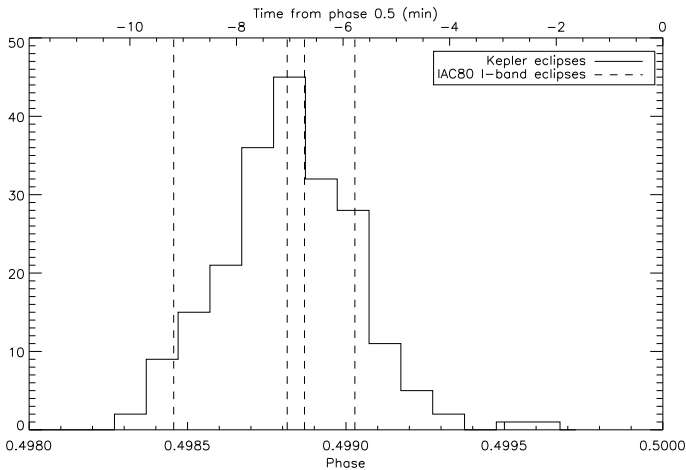


Fig. 4. Histogram of the secondary eclipse distribution in phase (lower axis) and in time (upper axis). All the secondary eclipses are systematically below phase 0.5. The vertical dashed lines show the position of the four IAC80 I_C -band secondary eclipses.

or fourth order polynomials to the points in each eclipse. The timings of the Kepler eclipses have relatively large uncertainties (~ 3 min) because the events are sparsely sampled, given the 29.4 minutes sampling rate of the long cadence Kepler data. In the case of the IAC80 light curves, which are better sampled, we fitted sixth order polynomials for both the primary and secondary eclipses. Times for the secondary eclipses were determined using the I_C -band light curve since it shows the deepest eclipses and allows a better determination of the minima. All the eclipse times are listed in Table 10.

To compute a new ephemerides equation for the system, we also added the eclipse times published by Devor et al. (2008a) and Çakırlı et al. (2013). When necessary, we converted the times of minima from HJD to BJD using the method of Eastman et al. (2010). We also conservatively assigned an uncertainty of 0.01 days to the eclipses of Devor et al. (2008a), given the dispersion of their photometry. All data combined provided a total of 228 primary eclipses over a time baseline of eight years. We fit all the measurements by a straight line, eliminating two of the Kepler observations, which presented long deviations caused by bad sampling of the eclipses. The result of that fit is the following updated ephemerides equation:

$$\text{MinI}(\text{BJD}) = 2455415.61831(5) + 4.1287955(4)n \quad (4)$$

The residuals to this fit show no signs of deviation from a straight line, which suggest no third body is present in the system, at least with orbital periods of the order of the observations timescale. Finally, we show a histogram with the phase distributions of the secondary eclipses in Fig. 4. All the eclipses are systematically below phase 0.5, with a mean phase of $\Delta\phi = 0.49894 \pm 0.00025$, which suggests that the binary is slightly eccentric.

5. Radial velocity and light curve fits

5.1. RV fitting procedure

We fit our RVs jointly with the primary and secondary measurements from Çakırlı et al. (2013) and Devor (2008). We fit a keplerian orbit to the data using the `rvfit` code (Iglesias-Marzoa et al. 2015). This code is based on an adaptive simulated annealing (ASA) algorithm and can simultaneously fit

Table 11. RV fitting results.

Parameter	Value
Adjusted Quantities	
P^a (d)	$4.1287955 \pm 4 \cdot 10^{-7}$
T_p (HJD)	2454936.705 ± 0.011
e^a	0.0365 ± 0.0014
ω^a (deg)	92.8 ± 2.2
γ (km/s)	-6.28 ± 0.53
K_1 (km/s)	48.07 ± 0.74
K_2 (km/s)	87.0 ± 2.5
Derived Quantities	
$M_1 \sin^3 i$ (M_\odot)	0.677 ± 0.046
$M_2 \sin^3 i$ (M_\odot)	0.374 ± 0.017
$q = M_2/M_1$	0.553 ± 0.018
$a_1 \sin i$ (10^6 km)	2.728 ± 0.042
$a_2 \sin i$ (10^6 km)	4.93 ± 0.14
$a \sin i$ (10^6 km)	7.66 ± 0.15
Other Quantities	
χ^2	58.657
χ_{red}^2	1.128
N_{obs} (primary)	47
N_{obs} (secondary)	9
Time span (days)	1507.86
rms_1 (km/s)	5.079
rms_2 (km/s)	3.492

Notes. ^(a) Parameter fixed beforehand.

the complete set of keplerian parameters [$P, T_p, e, \omega, \gamma, K_1, K_2$] for the primary and secondary RV curves by χ^2 function minimization. The uncertainties in the parameters can be computed from the Fisher matrix or using a Markov-Chain Monte Carlo method (MCMC). We chose this last method since it can deal with correlations between parameters. MCMC was run over 10^6 samples for each solution found with `rvfit`.

We ran a first fit to obtain initial parameter values and to check the significance of an elliptical orbit. In this first fit, we fixed only the orbital period to the value obtained in Sect. 4.6 and left all the other parameters free. This first solution was compatible with a low eccentricity, $e = 0.069 \pm 0.016$, orbit and a mass ratio of $q = 0.558 \pm 0.018$. This elliptical orbit is confirmed by the small displacement in phase of the secondary eclipses shown in Sect. 4.6.

The dispersion in the RV measurements and the sinusoidal appearance of the RV data distribution can hide the subtle effect of a small eccentricity. To circumvent this limitation, we decided to constrain the eccentricity and the argument of the periastron using the Kepler light curves (see Sect. 5.2) and fix them to the values $e = 0.0365 \pm 0.0014$ and $\omega = 92.8 \pm 2.2$ deg. This new fit yielded the values in Table 11. The fitted RV curve is shown in Fig. 5.

5.2. Light curves preliminary analysis with JKTEBOP

We used the detrended Kepler data to obtain an initial model of the light-curve without spots and to fix some initial parameters, namely $e \cos \omega$ and $e \sin \omega$. This allows us to start our combined analysis of the multiband light curves with initial values near the final solution once the spots are included in the analysis. For

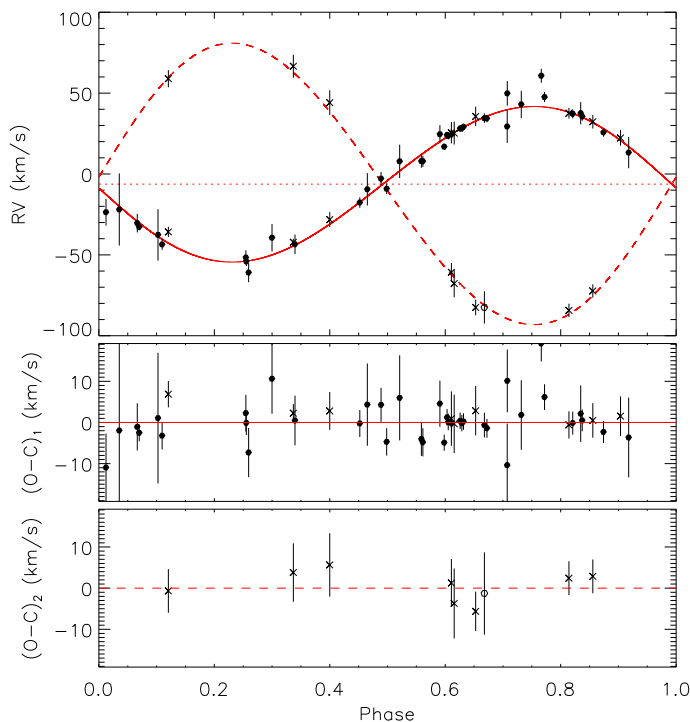


Fig. 5. RV curve fit and residuals. The continuous and dashed curves are the fits for the primary and secondary stars, respectively. The filled and empty circles are the RV measurements for the primary and secondary star respectively. The crosses are the RV measurements from Çakırlı et al. (2013). The dotted line in the upper panel is the value for γ . The phase was computed with Eq. 4.

this goal we used JKTEBOP² (Southworth et al. 2004), which is based on the EBOP code (Popper & Etzel 1981; Etzel 1981) and models the stars as triaxial ellipsoids. We fixed q , P and T_0 from the ephemeris Eq. 4, and the solution of the RV curves (Sect. 5.1). We fit the following parameters: the sum and ratio of fractional radii, i. e. $r_1 + r_2$ and r_1/r_2 , the orbital inclination i , the quantities $e \sin \omega$, $e \cos \omega$, the surface bright of the secondary, and the light scale factor.

In this first stage, the effect of heating between the two components of the binary was not taken into account, since it was eliminated from the light curves when we detrended the out-of-eclipse variations. Therefore, the model coefficients associated with this effect were fixed to zero. In any case, we ran tests to confirm this effect was not noticeable. The third light contribution, l_3 , was fixed to the value calculated in Sect. 4.5. Tests fitting l_3 yielded solutions with higher third light contributions, but poorer fits. We adopted a square-root limb darkening (LD) law (Diaz-Cordoves & Gimenez 1992; van Hamme 1993), with the LD coefficients interpolated from the tables provided by Claret & Bloemen (2011) and PHOENIX stellar models using the nominal T_{eff} of 5560 ± 160 K and 3350 ± 50 K for the primary and secondary components. We adopted those values running preliminary PHOEBE tests with the optical IAC80 curves and the RV solution for a circular orbit. The PHOENIX models were selected based in their lower T_{eff} limit, although the LD coefficient were computed only for $Z=0.0$. The $\log g$ values were set to 4.5 and 5.0 for each component, respectively. For the gravity-brightening coefficients we used values from Claret & Bloemen (2011) for the same T_{eff} .

² JKTEBOP is written in FORTRAN 77 and the source code is available at <http://www.astro.keele.ac.uk/~jktcodes/jktebop.html>

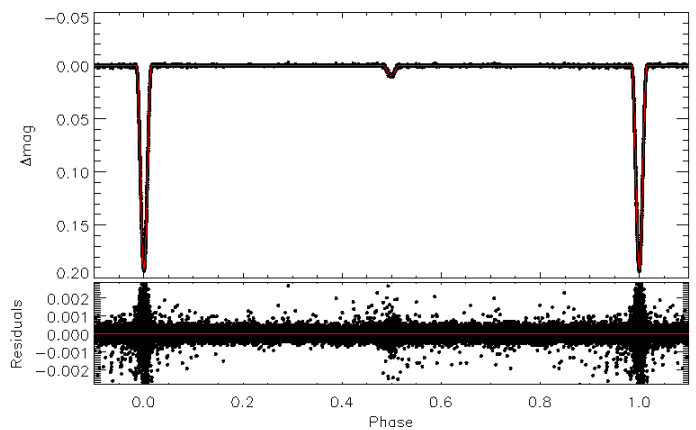


Fig. 6. JKTEBOP fit to the Kepler detrended light-curve. A detailed plot of the fits in the eclipses is shown in Fig. 7

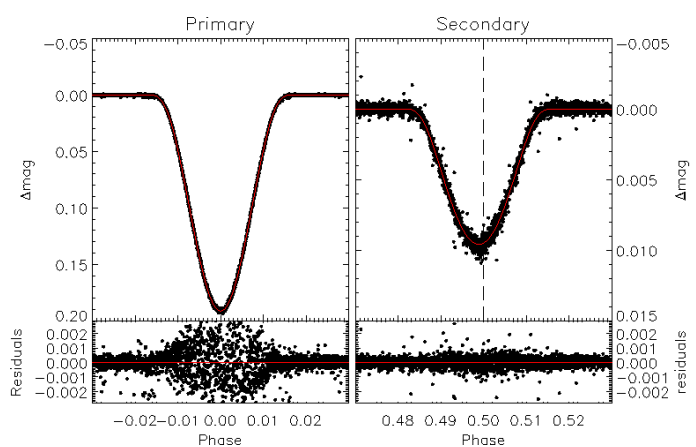


Fig. 7. Detail of the Fig. 6 showing the fit in the eclipses. Note the change in the vertical scale in the two plots and the small displacement of the secondary eclipse from phase 0.5, indicated with a vertical dashed line.

To avoid problems caused by the long integration time of the Kepler data, we split up each observation into six points to undergo a numerical integration. The effect of this Kepler long integration time in light curves of eclipsing binaries (Coughlin et al. 2011) and exoplanet systems (Kipping 2010) is a known issue. These authors find that undersampling affects the morphological shape of the eclipses (transits), in such a way that they appear to be shallower and have a longer duration. This effect is most pronounced in eclipsing binaries with short periods and low sum of the fractional radii ($r_1 + r_2$) values. T-Cyg1-12664, with a $r_1 + r_2 \simeq 0.1$ is in the range where this effect can be noticed.

The heavy detrending applied to the Kepler light curve produces points deviating largely from the model in phases with strong light curve curvature near the center of the eclipses (see Fig. 7). Thus, a conservative sigma-clipping of 10σ was applied in the fitting process to discard these points. With this preliminary fit, we arrived at the solution shown in Figs. 6 and 7, where $i = 86.87 \pm 0.14$, $e = 0.0365 \pm 0.0014$, and $\omega = 92.8 \pm 2.2$. The resulting fractional radii are $r_1 = 0.07282 \pm 0.00098$ and $r_2 = 0.03300 \pm 0.00050$. The uncertainties in the fitted parameter were computed using a bootstrap analysis with 5 000 synthetic datasets.

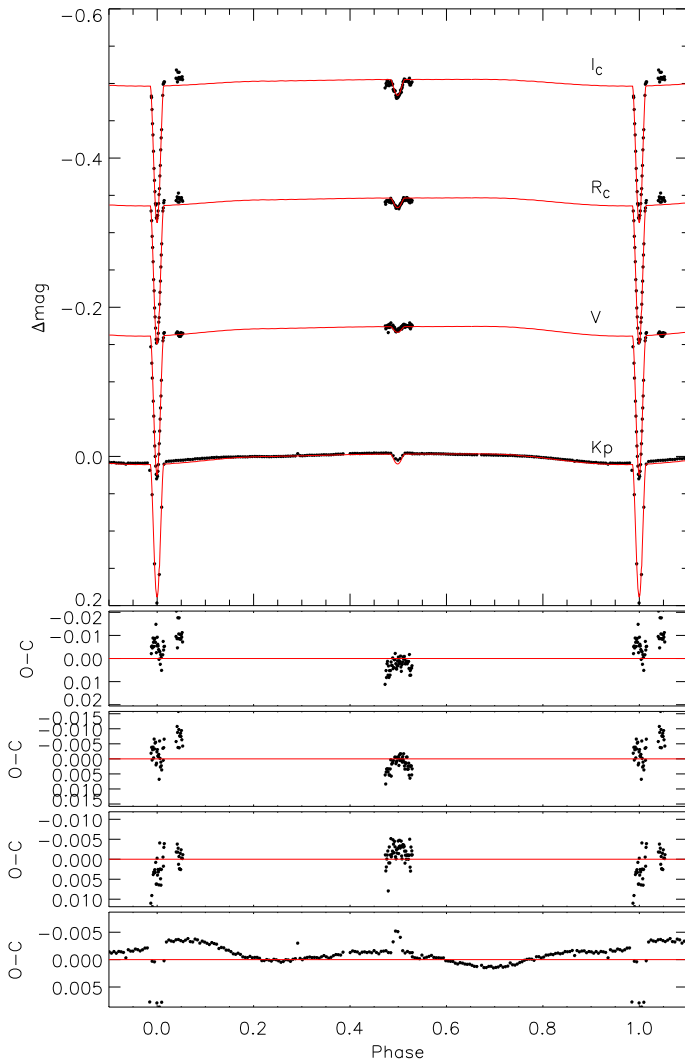


Fig. 8. Light curves of the T-Cyg1-12664 in the epoch Q6-1 and fitted model with the parameters of the first column in Table 12. From top to bottom, filters I_C , R_C , V , and Kepler band. The ground-based observations are displaced vertically to shrink the plot. The lower panels show the residuals of these fits in the same order.

5.3. Final light curve analysis with PHOEBE

To properly model the multiband light-curves of T-Cyg1-12664, we used PHysics Of Eclipsing BinariEs (PHOEBE, Prša & Zwitter 2005; Prša 2011). Given the low value of q for this system, the Roche lobe relative radii for each star (Eggleton 1983) are $r_{RL1} \simeq 0.43$ and $r_{RL2} \simeq 0.33$, well above the values obtained for the relative radii from the preliminary fit with JK-TEBOP, so we selected a detached eclipsing binary model in PHOEBE.

We fit the IAC80 $VR_C I_C$ light curves simultaneously with the Kepler light curve, but only using epochs of the Kepler light curve coeval with the ground-based observations. This is a necessary step to ensure that we are modeling the same spot configuration. Almost all IAC80 observations are coeval with Kepler’s Q6. We identified three epochs in which a primary and a contiguous secondary eclipses were observed simultaneously in all four bands. One epoch was discarded owing to unidentified systematics in the IAC80 data, which affect the level of the primary eclipse. The other two were selected for analysis with PHOEBE.

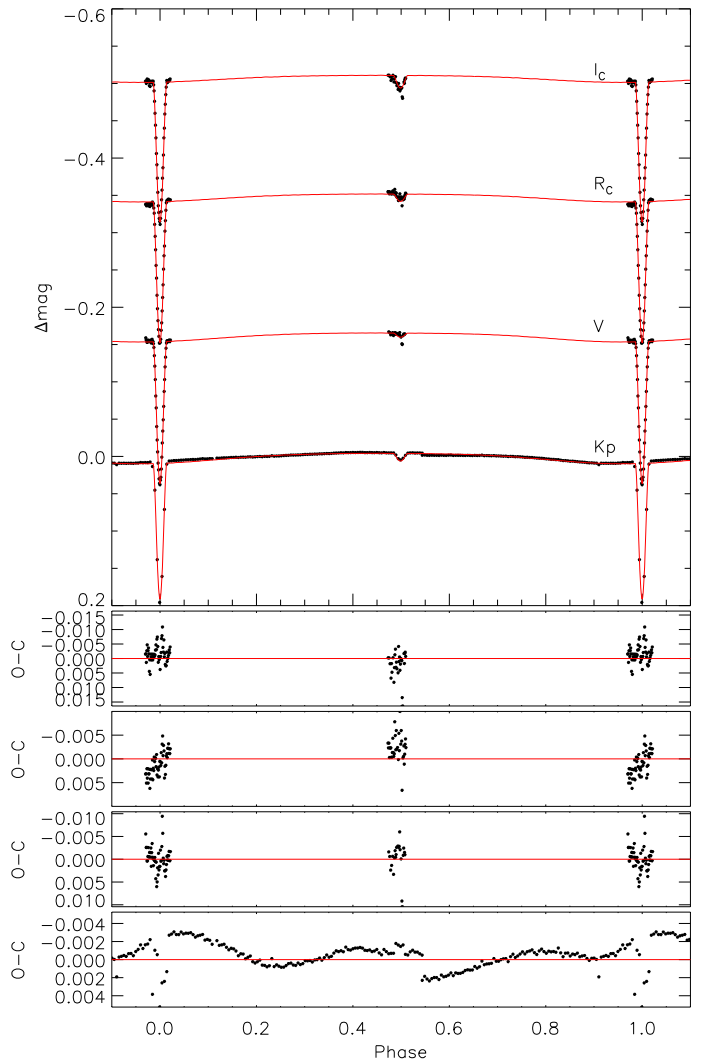


Fig. 9. Same figure as 8, but for the Q6-2 epoch. Note the jump in the Kepler photometry at phase 0.55 (see text).

To avoid potential problems introduced by the ≈ 28 min low-cadence duty cycle of the Kepler light-curve, we performed a first fit using only the IAC80 light curves and the initial parameters derived from the detrended Kepler light curve in Sect. 5.2 to get a first set of parameters for the binary (radius, effective temperatures, etc). With these results, we ran a new fit, this time including the Kepler light curve to properly model the spots. This two-step approach helps the fitting of the system because 1) the IAC80 $VR_C I_C$ light curves are best suited to constraining the effective temperatures, radii, and inclination of the system because of their high cadence during eclipses and finer spectral resolution and 2) the Kepler lightcurve have a better coverage of the out-of-eclipse phases, which allows us to model the spots. In the second fit, the physical and geometrical parameters of the binary are fixed and we only fit the spots. We iterate this two-step process until a satisfactory model is obtained and variations in the resultant parameters remain within the uncertainties for at least three consecutive fits. This approach has the disadvantage of being slower than the simultaneous fit of all the light curves but our preliminary test showed that the fitting results were notably better from the residuals point of view. The main advantage is that we retain both the physical information that are contained in the ground-based light curves and the excellent time coverage of the spot configuration contained in the Kepler light curves.

Table 12. T-Cyg1-12664 parameters computed for two different epochs.

Parameter	Q6-1 epoch	Q6-2 epoch
Time span	2455376.51579 - 2455380.64350	2455380.70480 - 2455384.83250
Geometric and orbital parameters		
P (d) (fixed)	4.1287955(7)	
T_0 (BJD) (fixed)	2455415.61831(5)	
$\Delta\phi$	-0.000800±0.000024	-0.000700±0.000023
q (fixed)	0.553±0.018	
γ (km s ⁻¹) (fixed)	-6.28±0.53	
i (deg)	87.003±0.012	86.931±0.010
e (fixed)	0.0365±0.0014	
a (R_\odot) (fixed)	11.03±0.21	
ω (deg) (fixed)	92.8±2.2	
Ω_1	14.391±0.057	14.257±0.038
Ω_2	19.461±0.072	18.937±0.061
F_1 (fixed)	1.041±0.024	
F_2 (fixed)	1.000	
Fractional volumetric radii		
r_{1vol}	0.07240±0.00060	0.07311±0.00040
r_{2vol}	0.03039±0.00024	0.03129±0.00022
Radiative parameters		
T_{eff1} (K) (fixed)	5560±160	
T_{eff2} (K)	3540±160	3380±160
Albedo (fixed)	0.5	
β_1, β_2	0.4353, 0.3710	0.4353, 0.3837
I_3^{Kp} (fixed)	0.02297±0.00058	
Limb-darkening coefficients (square-root law)		
x_1, y_1 (bol)	0.3811, 0.3636	0.3811, 0.3636
x_2, y_2 (bol)	-0.0427, 0.8284	-0.0427, 0.8284
x_1, y_1 (K_p band)	0.3598, 0.3869	0.3598, 0.3869
x_2, y_2 (K_p band)	0.0928, 0.8096	0.0628, 0.8721
x_1, y_1 (V band)	0.4786, 0.3242	0.4786, 0.3242
x_2, y_2 (V band)	0.1759, 0.7896	0.1544, 0.8349
x_1, y_1 (R_C band)	0.3177, 0.4299	0.3177, 0.4299
x_2, y_2 (R_C band)	0.1592, 0.7278	0.1061, 0.8169
x_1, y_1 (I_C band)	0.1795, 0.4965	0.1795, 0.4965
x_2, y_2 (I_C band)	-0.1726, 1.0385	-0.1848, 1.0833
Spot 1 parameters (primary star)		
Colatitude (deg)	81.3±7.4	19.51±7.4
Longitude (deg)	18.2±1.5	20.9±1.8
Radius (deg)	19.97±0.40	29.39±0.45
T_{spot}/T_{surf}	0.98141±0.00087	0.9686±0.0014
Spot 2 parameters (primary star)		
Colatitude (deg)	34.9±4.1	93±7.2
Longitude (deg)	286.31±7.3	291.8±9.0
Radius (deg)	14.5±0.66	8.1±1.5
T_{spot}/T_{surf}	0.9801±0.0047	0.9862±0.0037
Parameters computed from MCMC		
$\Delta\phi$	-0.00027 ^{+0.00028} _{-0.00024}	-0.00026 ^{+0.00030} _{-0.00027}
i (deg)	87.009 ^{+0.025} _{-0.030}	86.9291 ^{+0.0091} _{-0.0068}
Ω_1	14.48 ^{+0.48} _{-0.60}	14.30 ^{+0.70} _{-0.42}
Ω_2	18.97 ^{+0.28} _{-0.38}	18.64 ^{+0.45} _{-0.32}
T_{eff2} (K)	3548 ⁺³⁵ ₋₃₈	3365 ⁺⁴⁵ ₋₅₂
Fractional volumetric radii from MCMC		
r_{1vol}	0.0719 ^{+0.0024} _{-0.0032}	0.0729 ^{+0.0021} _{-0.0037}
r_{2vol}	0.0312 ^{+0.0014} _{-0.0010}	0.0318 ^{+0.0011} _{-0.0016}
Derived physical radii from MCMC		
R_1 (R_\odot)	0.793 ^{+0.030} _{-0.038}	0.804 ^{+0.028} _{-0.044}
R_2 (R_\odot)	0.344 ^{+0.017} _{-0.013}	0.351 ^{+0.014} _{-0.019}

Given the large number of parameters in a complete binary system model, we tried to fix as many of them as possible beforehand, using all available information. We fixed the period and T_0 to the values in the ephemeris equation in Sect. 4.6. The mass ratio q and γ were fixed from the RV solution in Table 11. The values for e and ω were fixed from the preliminary JKTEBOP analysis of the Kepler detrended light-curve in Sect. 2.1. The syn-

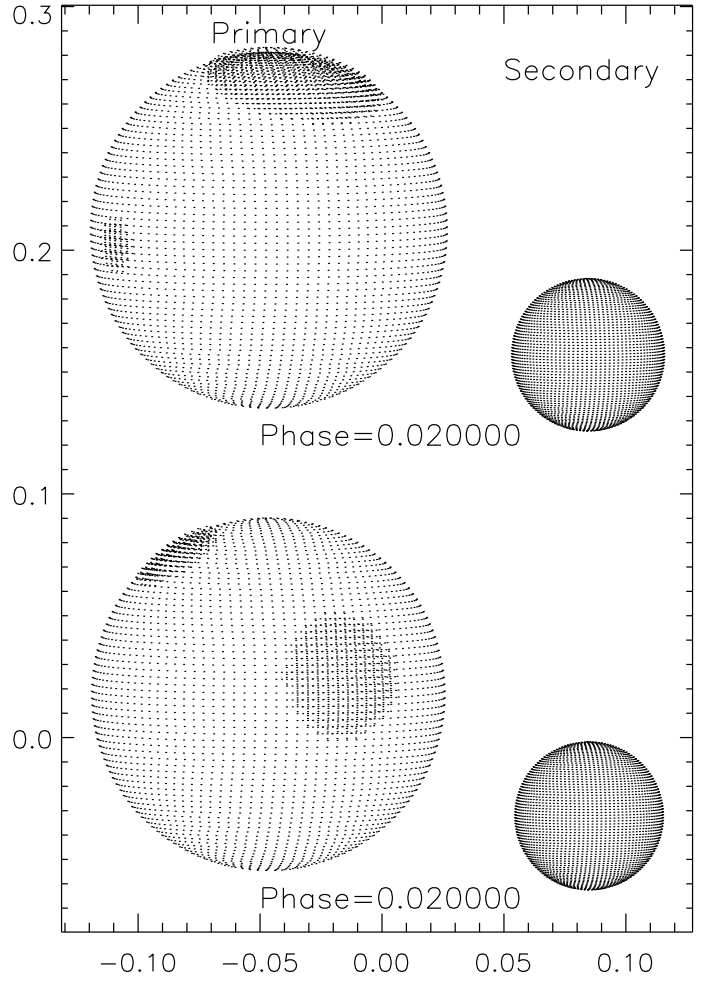


Fig. 10. Representation of the spot configurations of T-Cyg1-12664 in the (v, w) plane for the two epochs analyzed: the lower plot is for the Q6-1 epoch and the upper plot is for the Q6-2 epoch, which is displaced by an offset of 0.2 in the w axis. Both axes have units of relative radius. The stars are represented at orbital phase 0.020, just after the primary eclipse, and the secondary star is orbiting towards the right side.

chronicity parameter for the primary F_1 was set to 1.041 ± 0.024 , as obtained in Sect. 4.4. Although this is a very small value and it would not have practical effects on the shape of the star, we included it for completeness. For the secondary star, the synchronicity parameter F_2 was assumed to be 1.0.

T_{eff1} was set to 5560 ± 160 K, as computed in Sect. 4.2, in agreement with the spectroscopic value and the colors derived from the absolute photometry. The albedos of the two components were set to $A_1 = A_2 = 0.5$ as given by Ruciński (1969), since the temperatures and spectral types are compatible with those of stars with convective envelopes. The values of the gravity-brightening exponents, β_1 and β_2 , and those of the LD coefficients were interpolated from Claret & Bloemen (2011) for each passband. As in the case of the JKTEBOP preliminary light-curve analysis we used a square-root LD law (Diaz-Cordoves & Gimenez 1992). For the primary star these coefficient values were kept fixed since T_{eff1} does not change throughout the fitting process. For the secondary, we updated the coefficients values whenever necessary. As in Sect. 5.2, we used the same set of PHOENIX-based LD coefficients. This is because, during the fitting process, the T_{eff2} evolves below the 3500 K limit of the Kurucz LD tables. This occurred for all fitting attempts using the Phoebe(2010) or van Hamme (1993) LD

coefficients, pointing to a $T_{\text{eff}2}$ lower than 3500 K. This situation is most evident in the MCMC computations (see Sect. 5.5), some of them computing the merit function with T_{eff} well below the 3500 K limit for the secondary.

The third light in the Kepler band was set to the value computed in Sect. 4.5. For the VR_{CI} band we set it to 0 since there is no evidence of a third body in the system and our photometry excludes the nearby red star. Even so, we run preliminary tests to check this assumption by fitting third light. The results were compatible with $l_3=0$. For completeness, we also included mutual heating between the two components, but its effect is negligible in this system.

5.4. Spot modelling

A good spot model is critical for this system. Preliminary tests to decide on which component to place the spots showed that placing spots on the secondary had negligible effects on the light curve. This was expected, given the large difference in luminosity between the two components.

Our initial model consists of two spots on the primary located at phases $\phi \approx -0.05$ and $\phi \approx 0.20$ ($\lambda \approx 18^\circ$ and $\lambda \approx 288^\circ$), and at a latitude of $\sim 45^\circ$, since this is the latitude that some studies claim is more affected by spots (Hatzes 1995; Granzer et al. 2000). Our final spot solutions for the two epochs (see Figs. 8 and 9) show small deviations in the residuals with phase widths less than 0.5, so it cannot be produced by a single stellar spot. We tried to reduce these deviations by adding more spots to the primary without seeing significant improvements in the results. The Kepler light curve for the Q6-2 epoch shows a jump near phase $\phi \approx -0.55$, which prevents a better spot model fit, this jump is caused by small uncorrected drifts in the Kepler photometry, by the evolution in size or temperature of spots or by a combination of the two effects.

5.5. Final solutions

Taking into account the constraints and parameter values derived in the previous sections, the parameters fitted in the final model were the phase shift $\Delta\phi$, the secondary temperature $T_{\text{eff}2}$, the orbital inclination i , the two surface potentials Ω_1 , Ω_2 , the pass-band luminosities, and the spot parameters. The parameters common to the two columns were kept fixed during the fits and are the same for both epochs. For P and T_0 , the uncertainty is shown within parentheses. The final solutions for the two epochs analyzed are summarized in Table 12, while the fitted light curves and their residuals are shown in Figs. 8 and 9.

Additionally, we used an MCMC wrapper for PHOEBE to re-fit the parameter values and to obtain a better estimation of the uncertainties in those parameters. The results of this computation are shown at the end of Table 12, while Figures 11 and 12 show the parameter correlations from MCMC simulations and histograms of individual parameter distributions. To ensure the robustness of the fitted light curve model we ran a Gelman-Rubin diagnostics (Gelman & Rubin 1992) on the fitted parameters. Table 13 shows the \hat{R} values, all of them very near 1.0, which indicate a robust solution.

The fractional radii of each star are similar between the two epochs, but with differences slightly larger than the computed uncertainties. The departure from a perfectly spherical shape is very small ($\approx 0.07\%$ for the primary and $\approx 0.013\%$ for the secondary), as expected from the wide separation between the stars and their small masses. The position of the spots differs sig-

Table 13. Computed \hat{R} values from a Gelman-Rubin test for the fitted parameters in the two epochs analyzed.

Fitted parameter	Q6-1	Q6-2
$\Delta\phi$	1.01453	1.02198
$T_{\text{eff}2}$	1.02718	1.01771
i	1.01481	1.00577
Ω_1	1.01348	1.01559
Ω_2	1.02770	1.01063
HLA	1.00799	1.01104

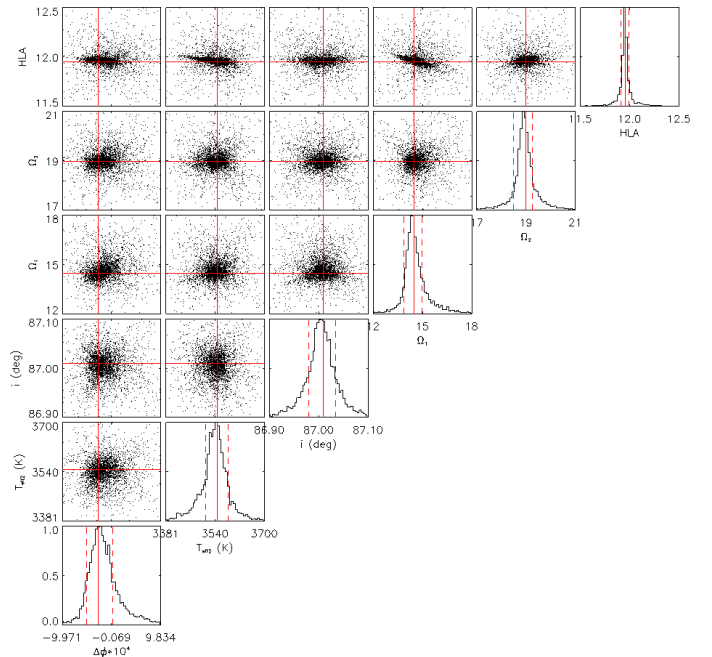


Fig. 11. Parameter correlations resulting from MCMC fit and histograms of individual parameter distributions for the Q6-1 epoch light curve. The red lines show the values adopted in this work from the maximum of the histograms. Dashed vertical lines indicated the 68.3% confidence interval.

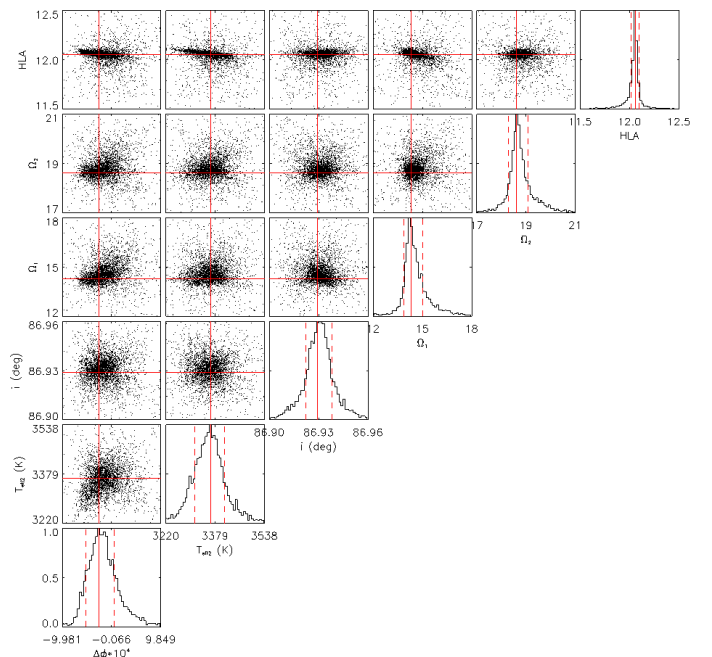


Fig. 12. Same as Fig. 11 but for the Q6-2 epoch light curve.

Table 14. Absolute dimensions and main physical parameters of the T-Cyg1-12664 system components.

Parameter	Primary	Secondary
Spectral type	G6V	M3V
Mass (M_{\odot})	0.680 ± 0.045	0.376 ± 0.017
Radius (R_{\odot})	0.799 ± 0.017^a	0.3475 ± 0.0081^a
$\log g$ (cgs)	4.465 ± 0.034	4.931 ± 0.028
T_{eff} (K)	5560 ± 160	3460 ± 210^a
$v_{\text{rot}} \sin i$ (km s $^{-1}$)	10.17 ± 0.32^b	-
$v_{\text{sync}} \sin i$ (km s $^{-1}$)	9.77 ± 0.21^c	4.25 ± 0.10^c
BC_V (mag)	-0.124 ± 0.037	-2.45 ± 0.78
L/L_{\odot}	0.550 ± 0.068	0.0156 ± 0.0039
M_{bol} (mag)	5.40 ± 0.13	9.26 ± 0.27
M_V (mag)	5.52 ± 0.14	11.71 ± 0.83

Notes. ^(a) Taken as the average of the MCMC values measured at the two epochs. ^(b) Computed from the spots rotation period. ^(c) Projected rotational velocity expected for synchronous rotation and a circular orbit.

nificantly between epochs, being the most stable parameter the longitude, which is tightly constrained by the light curve dips. The differences between models for T_{eff} and the radii could be related to this variation in the spots configuration, as noted by Morales et al. (2010). In Fig. 10, we show a representation of the spot configuration resulting from our analysis in the two epochs analyzed.

6. The system of T-Cyg1-12664

6.1. Absolute parameters

From the results in Tables 11 and 12, we computed the absolute parameters for the components of T-Cyg1-12664. Those results are summarized in Table 14. The adopted radii, T_{eff} and orbital inclination were computed from the mean for the two fits and their uncertainties are the standard deviations. The secondary is an M3V star, based on its effective temperature (Mamajek 2015). For the solar values we used the recommended IAU values $T_{\text{eff}\odot}=5772$ K, $\log g_{\odot}=4.438$, $M_{\text{bol}\odot}=4.74$ (IAU Inter-Division A-G Working Group on Nominal Units for Stellar and Planetary Astronomy 2015; Prša et al. 2016). The bolometric corrections were computed using the BC scale by Flower (1996) (but see Torres 2010, Sect. 2).

The uncertainties in the masses are 6.7% for M_1 and 4.5% for M_2 , which are consistent with the uncertainties in the RV amplitudes. The uncertainties in the radii are 2.1% for R_1 and 2.3% for R_2 . The radii are in good agreement with those obtained from the JKTEBOP model without spots (see Sect. 5.2), which resulted in $R_1=0.803 \pm 0.019 R_{\odot}$ and $R_2=0.364 \pm 0.0089 R_{\odot}$. The difference in the secondary radius can be attributed to the strong impact of the spots in the light curve, compared with the depth of the secondary eclipse. The orbit is nearly edge-on with an inclination of $i=86.969 \pm 0.056$ degrees, adopted from the mean of the two fits. The luminosity ratio in the visual band is $L_B/L_A = 0.0034 \pm 0.0026$ and its uncertainty reflects the uncertainty of the secondary absolute magnitude. Given the uncertainties in the T_{eff} scale, we adopted uncertainties of ± 1 in the spectral types.

Hut (1981) showed that, in a eccentric orbit, the rotational angular velocity of a star will tend to synchronize with the velocity at periastron as a consequence of the strong dependence of the tidal forces on distance, a condition called pseudosyn-

chronization. With the value of the orbital eccentricity, we computed the synchronicity parameter for the case of pseudosynchronization (Hut 1981, eq. 44) to be $F_{\text{pseudo}} = 1.0765 \pm 0.0031$, which is slightly larger than our measured synchronicity parameter $F = 1.041 \pm 0.024$. The difference could be due to differential rotation with spot latitude, in which case the spot's rotation would not be representative of the actual stellar rotation. In addition, the result from the Lomb-Scargle periodograms could be biased by the fact that there are, at least two groups of spots, making the resulting rotation period a mean of the movement of the two groups. Given the small eccentricity measured, we can consider that the orbit is circularized, and this will impose a lower limit for the age of the system because of the long time required to achieve this state. Using tidal friction theory Zahn (1977), we find the time scale for synchronization is $t_{\text{sync}} \approx 6$ Myr, and the time scale for circularization $t_{\text{circ}} \approx 2$ Gyr, which sets a minimum age for the system.

6.2. Distance, space velocities and age

Combining the absolute V magnitudes of the two components, we obtain an absolute V magnitude for T-Cyg1-12664 of $M_{V\text{tot}} = 5.52 \pm 0.14$. Given the apparent visual magnitude of the system $V = 13.299 \pm 0.005$ (see Sect. 4.1), this gives an unreddened distance modulus of $m-M=7.78$, which translates into a distance of $d = 360 \pm 22$ pc.

We computed the $(U, V, W)^3$ space velocities of the system using the Johnson & Soderblom (1987) algorithm, the distance computed above, the system's systemic velocity (see Sect. 5.1) and the 2MASS proper motion measurements (Cutri 2003): $\mu_{\alpha} \cos \delta = -18 \pm 6$ mas yr $^{-1}$, $\mu_{\delta} = -6 \pm 2$ mas yr $^{-1}$. The resultant velocities are $U = 17.5 \pm 3.3$ km s $^{-1}$, $V = -11.1 \pm 1.7$ km s $^{-1}$, $W = 11.5 \pm 5.9$ km s $^{-1}$, and a total space velocity of $S = 23.7 \pm 7.0$ km s $^{-1}$. These velocities place the binary near the border of the area defined by Eggen (1989) as belonging to the young galactic disk. The velocities do not exactly agree with the criteria of Leggett (1992) ($-50 < U < 20$, $-30 < V < 0$, $-25 < W < 10$, all in km s $^{-1}$) but they lie very near the limit. Also the binary is not within any known early-type or late-type population tracer (Skuljan et al. 1999), although it lies near the V-middle branch for late-type stars ($U=17.8$, $V=-15.37$) km s $^{-1}$. This relation may also be related to any known moving group (Montes et al. 2001; Maldonado et al. 2010). Therefore, we cannot impose constraints on the age of the system based on kinematic criteria. However, based on circularization and synchronization times for a $P \approx 4.13$ days orbit, we can speculate on an age of at least 2 Gyrs for the system. This age rules out the possibility of T-Cyg1-12664 being pre-main-sequence, and is a clue that its components are main-sequence stars.

In Fig. 13, we plotted the Baraffe et al. (1998) (hereafter BCAH98) isochrones for $[M/H]=0.0$ (in black) and for $[M/H]=-0.5$ (in red). All the isochrones older than $\log(\text{age})=8.0$ fit equally well the components of this system. The primary is better fitted by isochrones for $[M/H]=-0.5$, and the secondary is better fitted by isochrones for $[M/H]=0.0$. The effect of the subsolar metallicity could explain the primary's effective temperature, but not its oversize. However, the difference in the space parameter for the two sets of isochrones for the two metallicities is smaller than the uncertainties in the computed stellar parameters, and the uncertainty about the actual metallicity of the system remains. A specific metallicity analysis for this system would resolve this

³ Positive values of U , V , and W indicate velocities toward the Galactic center, Galactic rotation, and north Galactic pole, respectively.

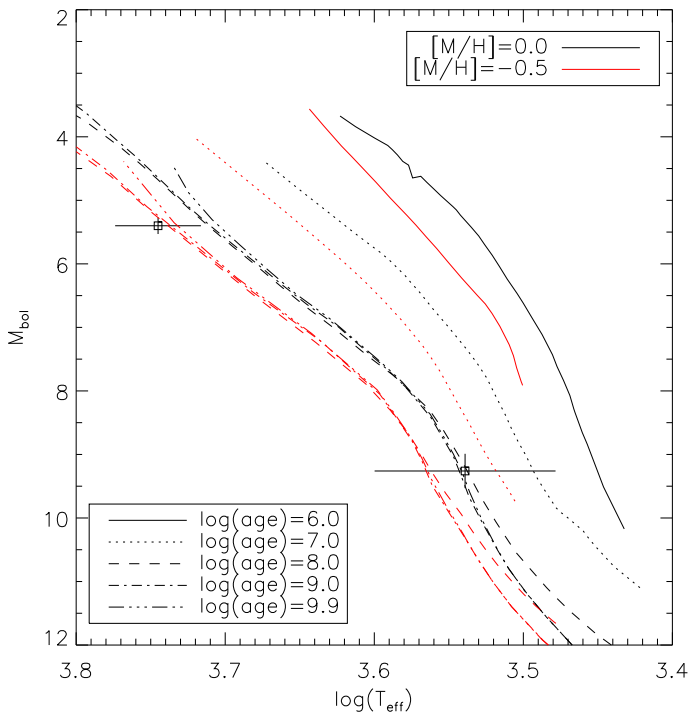


Fig. 13. Position in the $M_{\text{bol}}\text{-log } T_{\text{eff}}$ diagram of the two components in the system of T-Cyg1-12664. BCAH98 isochrones are for $[M/H]=0.0$ (black) and $[M/H]=-0.5$ (red) for $\log(\text{age})=6.0, 7.0, 8.0, 9.0$ and 9.9 .

question. All that can be said is that this system is old and we can safely discard a young pre-main-sequence system.

6.3. Comparison with models and previous analyses

Low-mass stars in eclipsing binaries are commonly found to have larger radii and lower effective temperatures than those predicted by current models. In Figs. 14 and 15, we compare the mass, radius, and temperature of the components of T-Cyg1-12664 to models and to other binaries. The models in the figures are those of Baraffe et al. (1998), Dotter et al. (2008), Girardi et al. (2000), and Yi et al. (2001), all of them for solar metallicity ($Z=0.02$) and an age of 3 Gyr, which cover the entire low-mass regime. We adopt those values since they provide a good fit to the overall sample of mass-radius measurements of main sequence low-mass stars in the literature, and also the secondary of T-Cyg-12664, although not the primary. We note, however, that this model is used for illustration of the entire observational sample of low-mass stars, and is not a fit to the T-Cyg-12664.

The mixing length parameter for the Baraffe et al. (1998) model is $\alpha = l/H_p = 1$. The other binaries included in the figure (listed in Table 15) are all the current systems with masses and radii measured with relative precisions better than 7%. We also included the previous measurements by Çakırlı et al. (2013) for this system in the figures.

Our results show agreement between the parameters of the secondary and models, in particular with the predictions from Baraffe et al. (1998) and Dotter et al. (2008). This is a particularly important result, since the secondary has a mass very close to the fully convective stellar boundary at $\sim 0.35 M_{\odot}$. The parameters of the primary, on the other hand, deviate significantly from the model predictions, both in the mass-radius and the mass- $\log T_{\text{eff}}$ plots. The primary is oversized $\sim 34\%$ over the value of

the radius predicted by the models. This deviation is larger than any other well measured binary components in this mass range. In the mass- $\log T_{\text{eff}}$ plane, the primary exhibits a very high effective temperature, being over 1000K hotter than what models for a star of that mass predict. We must emphasize that the temperature has been measured directly from the photometric colors, which are found to be consistent among photometric systems, and spectroscopy (see Sects. 4.2 and 4.3), and is not a result of the modeling process. At present, we can not find an explanation for this discrepancy, but there is at least one other low-mass binary that exhibits this effect (see Gómez Maqueo Chew et al. 2014).

Our results also differ from those of Çakırlı et al. (2013), the main differences in the analysis being the setting of a reliable set of color indexes, the treatment of the eccentricity, and the processing of the Kepler light curves. These differences can explain the disagreement in the parameters obtained from the light curves, i.e. the radii, the T_{eff} , and luminosity-related quantities. Only the masses, derived from the RV curves, are similar, although our secondary mass is slightly larger. We attribute this to improvements in the RV curve of the primary and the detection of a slight eccentricity for the system.

T-Cyg1-12664 was also analyzed by Prša et al. (2011) using Eclipsing Binaries via Artificial Intelligence (EBAI, Prša et al. 2008) on a survey of eclipsing binaries found in the Kepler field of view. EBAI relies on trained neural networks to yield principal parameters for all the binary stars in the catalog. In the accompanying table, we found the following values: $T_{\text{eff}}=5669$ K, $\log g=4.308$, $\sin i=0.99441$, $e \sin \omega=0.04452$, $e \cos \omega=-0.35923$, $T_2/T_1=0.5965$, and $\rho_1 + \rho_2=0.10881$, with an effective temperature in reasonable agreement with the value obtained from our photometry. The same authors published the Kepler Eclipsing Binary Catalog⁴ (KEB) online. A query of this catalog using the Kepler name of the system (KIC 10935310) returns a different set of physical parameters: $\sin i=0.99479$, $e \sin \omega=0.05606$, $e \cos \omega=0.22161$, $T_2/T_1=0.78209$, and $\rho_1 + \rho_2=0.13246$. The values for e and ω arising from both solutions are incompatible with our radial velocity and photometric curves. However, a new analysis of the Kepler dataset by the Kepler EB team gives $\omega=94.2$ degrees and $e=0.0372$, which are consistent with our values (Prša, priv. comm.).

7. Conclusions

Our analysis of the T-Cyg1-12664 low-mass eclipsing binary system shows a different picture from other published analyses (Devor 2008; Çakırlı et al. 2013). The main differences between our analysis and the previous ones are: the measurement of consistent and accurate calibrated magnitudes in the optical bands, which lead to a precise determination of the T_{eff} scale; a careful treatment of the contamination by nearby stars in the Kepler band photometry, with a direct impact in the orbital inclination and, thus, in the fractional radii; and the discovery of a small displacement of the secondary eclipse which lead to the analysis of the system as an eccentric binary.

Our results for this system show an oversized primary with $M_1 = 0.680 \pm 0.045 M_{\odot}$, $R_1 = 0.799 \pm 0.017 R_{\odot}$, and $T_{\text{eff}1} = 5560 \pm 160$ K, in a slightly eccentric orbit with $e = 0.0365 \pm 0.0014$ and $i = 86.969 \pm 0.056$. The secondary is a star near the fully convective stellar mass boundary with $M_2 = 0.376 \pm 0.017 M_{\odot}$, $R_2 = 0.3475 \pm 0.0081 R_{\odot}$, and $T_{\text{eff}2} = 3460 \pm 210$ K. Its parameters agree well with models.

⁴ Available at <http://keplerebs.villanova.edu/v2>.

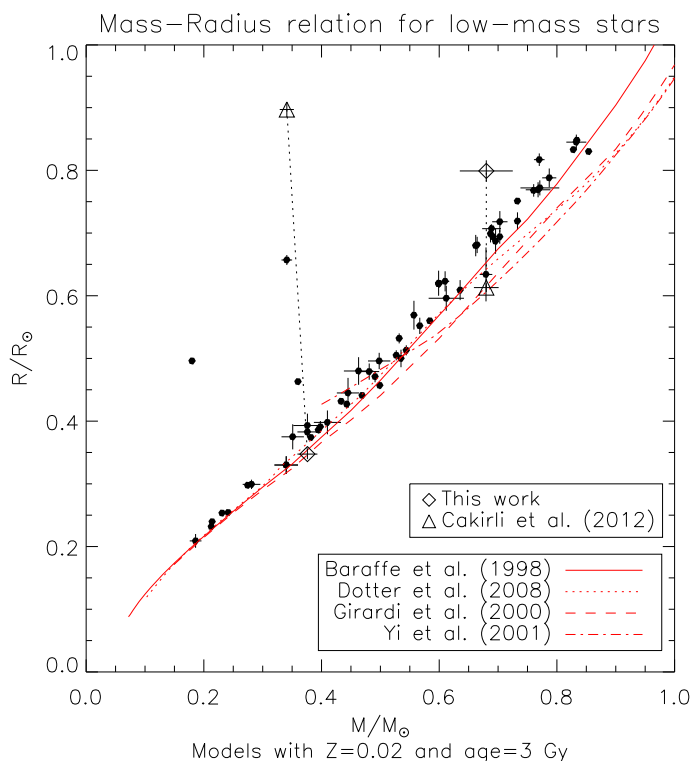


Fig. 14. Mass-radius relations of stars between 0.2 and 1.0 M_{\odot} predicted by four stellar models (see text). The filled circles represent well-known LMDEB, used as benchmarks for the models. The triangles represent the location of T-Cyg1-12664 in the Çakırlı et al. (2013) paper and the diamonds are our solution for this system. We connect the two solutions for the primary and the secondary with a dotted line to guide the eye to the difference in the physical parameters that arise from the two solutions. Metallicity and age are set for reference of the whole set of stars and they are not a fit to the T-Cyg1-12664 parameters.

The faintness of the secondary component is a drawback in the measurement of radial velocities for this system, which only shows the radial velocities of the primary with telescopes of medium size. This prevents us from directly measuring q for this system and forces us to rely on published radial velocities for the secondary. The secondary star appears to have a mass in a key region for models, i.e. the transition to fully convective stars, which remains poorly sampled by observations. Therefore, new measurements of the secondary radial velocity curve of this system using, for example, near-IR spectroscopy will be important.

Acknowledgements. We thank the referee A. Prša for helpful comments on the manuscript. This article is based on observations made with the IAC80 telescope operated on the island of Tenerife by the Instituto de Astrofísica de Canarias in the Spanish Observatorio del Teide, on observations obtained with the Apache Point Observatory 3.5-meter telescope, which is owned and operated by the Astrophysical Research Consortium, and on observations at Kitt Peak National Observatory, National Optical Astronomy Observatory (NOAO Prop. IDs: 2011A-0392; PI: J. Coughlin), which is operated by the Association of Universities for Research in Astronomy (AURA) under cooperative agreement with the National Science Foundation. IRAF is distributed by the National Optical Astronomy Observatory, which is operated by the Association of Universities for Research in Astronomy (AURA) under a cooperative agreement with the National Science Foundation. This research has made use of the SIMBAD database, operated at CDS, Strasbourg, France, and of NASA's Astrophysics Data System Bibliographic Services. Also, it used data products from the Two Micron All Sky Survey. Some of the data presented in this paper were obtained from the Mikulski Archive for Space Telescopes (MAST). This paper includes data collected by the Kepler mission. Funding for the Kepler mission is provided by the NASA Science Mission directorate. R.I.M. acknowledges support through the Programa de

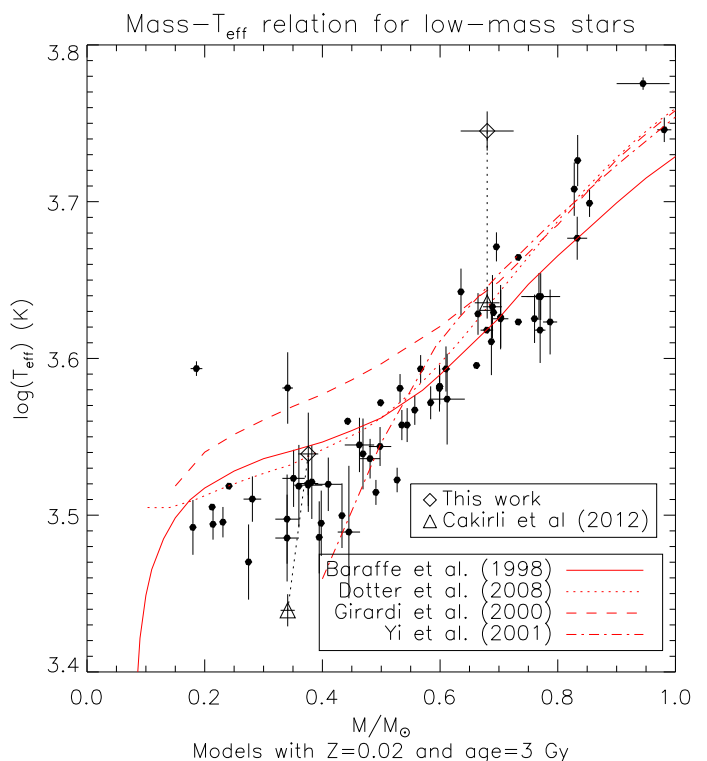


Fig. 15. Mass- $\log T_{\text{eff}}$ relations for the same LMDEB systems as in Fig. 14. Again, we connected with a dotted line the solutions derived by Çakırlı et al. (2013) for the primary and secondary with our solutions. Metallicity and age are set for reference of the whole set of stars and they are not a fit to the T-Cyg1-12664 parameters.

Acceso a Instalaciones Científicas Singulares (E/309290). J.L.C. acknowledges support through a National Science Foundation Graduate Research Fellowship.

References

- Alonso, R., Brown, T. M., Torres, G., et al. 2004, *ApJ*, 613, L153
Arribas, S. & Martínez Roger, C. 1988, *A&A*, 206, 63
Ballesteros, F. J. 2012, *EPL (Europhysics Letters)*, 97, 34008
Baraffe, I., Chabrier, G., Allard, F., & Hauschildt, P. H. 1998, *A&A*, 337, 403
Bayless, A. J. & Orosz, J. A. 2006, *ApJ*, 651, 1155
Behr, B. B. 2003, *ApJS*, 149, 67
Bessell, M. S. 1979, *PASP*, 91, 589
Bessell, M. S. 1991, *AJ*, 101, 662
Birkby, J., Nefs, B., Hodgkin, S., et al. 2012, *MNRAS*, 426, 1507
Brogna, P. 2006, PhD thesis, San Francisco State University
Brown, T. M., Latham, D. W., Everett, M. E., & Esquerdo, G. A. 2011, *AJ*, 142, 112
Çakırlı, Ö. 2013, *New A*, 22, 15
Çakırlı, Ö., İbanoğlu, C., & Sipahi, E. 2013, *MNRAS*, 429, 85
Carter, J. A., Fabrycky, D. C., Ragozzine, D., et al. 2011, *Science*, 331, 562
Claret, A. & Bloemen, S. 2011, *A&A*, 529, A75
Clausen, J. V., Bruntt, H., Claret, A., et al. 2009, *A&A*, 502, 253
Coughlin, J. L. 2012, PhD thesis, New Mexico State University
Coughlin, J. L., López-Morales, M., Harrison, T. E., Ule, N., & Hoffman, D. I. 2011, *AJ*, 141, 78
Cox, A. N. 2000, *Allen's Astrophysical Quantities*, 4th edn. (New York: AIP)
Cutri, R.M., et al. 2003, *The IRSA 2MASS All-Sky Point Source Catalogue*, Tech. rep., NASA/IPAC Infrared Science Archive, available at <http://irsa.ipac.caltech.edu/applications/Gator/>
Devor, J. 2008, PhD thesis, Harvard University
Devor, J., Charbonneau, D., O'Donovan, F. T., Mandushev, G., & Torres, G. 2008a, *AJ*, 135, 850
Devor, J., Charbonneau, D., Torres, G., et al. 2008b, *ApJ*, 687, 1253
Diaz-Cordoves, J. & Gimenez, A. 1992, *A&A*, 259, 227
Dotter, A., Chaboyer, B., Jevremović, D., et al. 2008, *ApJS*, 178, 89
Eastman, J., Siverd, R., & Gaudi, B. S. 2010, *PASP*, 122, 935
Eggen, O. J. 1989, *PASP*, 101, 366

- Eggleton, P. P. 1983, *ApJ*, 268, 368
- Eisenstein, D. J., Weinberg, D. H., Agol, E., et al. 2011, *AJ*, 142, 72
- Etzel, P. B. 1981, in *Photometric and Spectroscopic Binary Systems*, ed. E. B. Carling & Z. Kopal, 111
- Everett, M. E., Howell, S. B., & Kinemuchi, K. 2012, *PASP*, 124, 316
- Flower, P. J. 1996, *ApJ*, 469, 355
- Fukugita, M., Yasuda, N., Doi, M., Gunn, J. E., & York, D. G. 2011, *AJ*, 141, 47
- Gelman, A. & Rubin, D. 1992, *Statistical Science*, 7, 457
- Girardi, L., Bressan, A., Bertelli, G., & Chiosi, C. 2000, *A&AS*, 141, 371
- Gómez Maqueo Chew, Y., Morales, J. C., Faedi, F., et al. 2014, *A&A*, 572, A50
- Granger, T., Schüssler, M., Caligari, P., & Strassmeier, K. G. 2000, *A&A*, 355, 1087
- Hatzes, A. P. 1995, in *IAU Symposium*, Vol. 176, *IAU Symposium*, 90P
- Helminiak, K. G., Brahm, R., Ratajczak, M., et al. 2014, *A&A*, 567, A64
- Helminiak, K. G. & Konacki, M. 2011, *A&A*, 526, A29
- Helminiak, K. G., Konacki, M., RóŻyczka, M., et al. 2012, *MNRAS*, 425, 1245
- Helminiak, K. G., Konacki, M., Złoczewski, K., et al. 2011, *A&A*, 527, A14
- Houdashelt, M. L., Bell, R. A., & Sweigart, A. V. 2000, *AJ*, 119, 1448
- Hut, P. 1981, *A&A*, 99, 126
- IAU Inter-Division A-G Working Group on Nominal Units for Stellar & Planetary Astronomy. 2015, Resolution B2 on recommended zero points for the absolute and apparent bolometric magnitude scales, Tech. rep., IAU
- Iglesias-Marzoa, R., López-Morales, M., & Jesús Arévalo Morales, M. 2015, *PASP*, 127, 567
- Irwin, J., Charbonneau, D., Berta, Z. K., et al. 2009, *ApJ*, 701, 1436
- Irwin, J. M., Quinn, S. N., Berta, Z. K., et al. 2011, *ApJ*, 742, 123
- Ivezić, Ž., Sesar, B., Jurić, M., et al. 2008, *ApJ*, 684, 287
- Jenkins, J. M., Caldwell, D. A., Chandrasekaran, H., et al. 2010, *ApJ*, 713, L87
- Johnson, D. R. H. & Soderblom, D. R. 1987, *AJ*, 93, 864
- Kipping, D. M. 2010, *MNRAS*, 408, 1758
- Kraus, A. L., Tucker, R. A., Thompson, M. I., Craine, E. R., & Hillenbrand, L. A. 2011, *ApJ*, 728, 48
- Kurucz, R. L. 1993, *The 1993 Kurucz Stellar Atmospheres Atlas*, available at <ftp://ftp.stsci.edu/cdbs/grid/kurucz93models>
- Landolt, A. U. 2009, *AJ*, 137, 4186
- Lanza, A. F., Das Chagas, M. L., & De Medeiros, J. R. 2014, *A&A*, 564, A50
- Leggett, S. K. 1992, *ApJS*, 82, 351
- Lejeune, T., Cuisinier, F., & Buser, R. 1998, *A&AS*, 130, 65
- López-Morales, M. & Bonanos, A. Z. 2008, *ApJ*, 685, L47
- López-Morales, M. & Ribas, I. 2005, *ApJ*, 631, 1120
- Maldonado, J., Martínez-Arnáiz, R. M., Eiroa, C., Montes, D., & Montesinos, B. 2010, *A&A*, 521, A12
- Mamajek, E. E. 2015, *A Modern Mean Stellar Color and Effective Temperature Sequence for O9V-Y0V Dwarf Stars*, available at http://www.pas.rochester.edu/~emamajek/EEM_dwarf_UBVIJHK_colors_Teff.txt
- Masana, E., Jordi, C., & Ribas, I. 2006, *A&A*, 450, 735
- Merline, W. J. & Howell, S. B. 1995, *Experimental Astronomy*, 6, 163
- Montes, D., López-Santiago, J., Gálvez, M. C., et al. 2001, *MNRAS*, 328, 45
- Morales, J. C., Gallardo, J., Ribas, I., et al. 2010, *ApJ*, 718, 502
- Morales, J. C., Ribas, I., Jordi, C., et al. 2009a, *ApJ*, 691, 1400
- Morales, J. C., Torres, G., Marschall, L. A., & Brehm, W. 2009b, *ApJ*, 707, 671
- Moro, D. & Munari, U. 2000, *A&AS*, 147, 361
- Munari, U., Sordo, R., Castelli, F., & Zwitter, T. 2005, *A&A*, 442, 1127
- Popper, D. M. & Etzel, P. B. 1981, *AJ*, 86, 102
- Prša, A., Batalha, N., Slawson, R. W., et al. 2011, *AJ*, 141, 83
- Prša, A., Guinan, E. F., Devinney, E. J., et al. 2008, *ApJ*, 687, 542
- Prša, A., Harmanec, P., Torres, G., et al. 2016, *AJ*, 152, 41
- Prša, A. & Zwitter, T. 2005, *ApJ*, 628, 426
- Prša, A. 2011, *PHOEBE Scientific Reference*
- Reinhold, T. & Arlt, R. 2015, *A&A*, 576, A15
- Ribas, I. 2003, *A&A*, 398, 239
- Rozyczka, M., Kaluzny, J., Pietrukowicz, P., et al. 2009, *Acta Astron.*, 59, 385
- Ruciński, S. M. 1969, *Acta Astron.*, 19, 245
- Scargle, J. D. 1982, *ApJ*, 263, 835
- Skrutskie, M. F., Cutri, R. M., Stiening, R., et al. 2006, *AJ*, 131, 1163
- Skuljan, J., Hearnshaw, J. B., & Cottrell, P. L. 1999, *MNRAS*, 308, 731
- Slawson, R. W., Prša, A., Welsh, W. F., et al. 2011, *AJ*, 142, 160
- Southworth, J., Maxted, P. F. L., & Smalley, B. 2004, *MNRAS*, 351, 1277
- Torres, G. 2010, *AJ*, 140, 1158
- Torres, G. & Ribas, I. 2002, *ApJ*, 567, 1140
- Vaccaro, T. R., Rudkin, M., Kawka, A., et al. 2007, *ApJ*, 661, 1112
- van Dokkum, P. G. 2001, *PASP*, 113, 1420
- van Hamme, W. 1993, *AJ*, 106, 2096
- Yi, S., Demarque, P., Kim, Y.-C., et al. 2001, *ApJS*, 136, 417
- Zahn, J.-P. 1977, *A&A*, 57, 383
- Zucker, S. & Mazeh, T. 1994, *ApJ*, 420, 806
- Östensen, R. 2000, PhD thesis, University of Trondheim
- Östensen, R. & Solheim, J.-E. 2000, *Baltic Astronomy*, 9, 411

Table 1. Detrended Kepler light curve for T-Cyg1-12664. Full version of this table is available in electronic form at the CDS.

BJD day	Normalized flux –
2454954.43757	1.0000260
2454954.45800	0.99973979
2454954.47843	1.0001384
...	

Table 2. IAC80 differential photometry for T-Cyg1-12664. Full version of this table is available in electronic form at the CDS.

BJD day	Δm mag	Error mag	Airmass –	Filter –
2455378.404710830	1.603	0.001	1.825	V
2455378.407322901	1.671	0.001	1.796	Rc
2455378.409550562	1.767	0.001	1.771	Ic
...				

Table 3. Measured RV for the primary component in the T-Cyg1-12664 system. Full version of this table is available in electronic form at the CDS.

BJD day	RV1 km s ⁻¹	error km s ⁻¹
2455426.823697	49.82	7.61
2455447.710532	60.73	4.36
2455450.826485	7.83	10.32
...		

Table 10. Measured times of minima for T-Cyg1-12664. Full version of this table is available in electronic form at the CDS.

BJD day	Error day	Minimum Type –	Reference –
2453177.81205	0.00100	P	1
2453181.93795	0.00100	P	1
2453206.71285	0.00100	P	1
...			

References. (1) Devor et al. (2008a); (2) IAC80 data; (3) Kepler data; (4) Çakırlı et al. (2013)

Table 15. List of benchmark low-mass components in eclipsing binaries taken from the literature. The measured masses and radii have relative uncertainties less or equal 7%.

Component of binary	$M (M_{\odot})$	$R (R_{\odot})$	$T_{\text{eff}} \text{ (K)}$	References
YY Gem A/B	0.5992±0.0047	0.6191±0.0057	3820±100	1
V818 Tau B	0.7605±0.0062	0.768±0.010	4220±150	1
CU Cnc A	0.4333±0.0017	0.4317 ±0.0052	3160±150	2
CU Cnc B	0.3980±0.0014	0.3908±0.0094	3125±150	2
GU Boo A	0.610±0.007	0.623±0.016	3920±130	3
GU Boo B	0.599±0.006	0.620±0.020	3810±130	3
CM Dra A	0.2310±0.0009	0.2534±0.0019	3130±70	4
CM Dra B	0.2141±0.0010	0.2396±0.0015	3120±70	4
IM Vir A	0.981±0.012	1.061±0.016	5570±100	5
IM Vir B	0.6644±0.0048	0.681±0.013	4250±130	5
2MASS J05162881+2607387 A	0.787±0.012	0.788±0.015	4200±200	6
2MASS J05162881+2607387 B	0.770±0.009	0.817±0.010	4150±20	6
T-Lyr1-17236 A	0.6795±0.0107	0.634±0.043	4150	7
T-Lyr1-17236 B	0.5226±0.0061	0.525±0.052	3700	7
LSPM J1112+7626 A	0.3946±0.0023	0.3860±0.0055	3061±162	8
LSPM J1112+7626 B	0.2745±0.0012	0.2978±0.0049	2952±163	8
GJ 3236 A	0.376±0.017	0.3828±0.0072	3313±110	9
GJ 3236 B	0.281±0.015	0.2992±0.0075	3238±108	9
V636 Cen B	0.854±0.003	0.830±0.004	5000±100	10
NSVS 07394765 A	0.360±0.005	0.463±0.004	3300±200	11
NSVS 07394765 B	0.180±0.004	0.496±0.005	3106±125	11
NGC2204-S892 A	0.733±0.005	0.719±0.014	4200	12
NGC2204-S892 B	0.662±0.005	0.680±0.017	3940±20	12
RX J0239.1-1028 A	0.733±0.002	0.751±0.002	4618±14	13
RX J0239.1-1028 B	0.691±0.002	0.694±0.003	4258±14	13
19b-2-01387 A	0.498±0.019	0.496±0.013	3498±100	14
19b-2-01387 B	0.481±0.017	0.479±0.013	3436±100	14
19c-3-01405 A	0.410±0.023	0.398±0.019	3309±130	14
19c-3-01405 B	0.376±0.024	0.393±0.019	3305±130	14
19e-3-08413 A	0.463±0.025	0.480±0.022	3506±140	14
19e-3-08413 B	0.351±0.019	0.375±0.020	3338±140	14
KOI-126 B	0.2413±0.0030	0.2543±0.0014	3300	15
KOI-126 C	0.2127±0.0026	0.2318±0.0013	3200	15
LP 133-373 A	0.340±0.020	0.330±0.014	3058±195	16
LP 133-373 B	0.340±0.020	0.330±0.014	3144±206	16
ASAS J011328–3821.1 Aa	0.612±0.030	0.596±0.020	3750±250	17
ASAS J011328–3821.1 Ab	0.445±0.019	0.445±0.024	3085±300	17
ASAS J045304-0700.4 A	0.8338±0.0036	0.848±0.005	5324±200	18
ASAS J045304-0700.4 B	0.8280±0.0040	0.833±0.005	5105±200	18
ASAS J082552-1622.8 A	0.7029±0.0045	0.694±0.011	4230±200	18
ASAS J082552-1622.8 B	0.6872±0.0049	0.699±0.014	4080±200	18
ASAS J093814-0104.4 A	0.771±0.033	0.772±0.012	4360±150	19
ASAS J093814-0104.4 B	0.768±0.021	0.769±0.012	4360±150	19
ASAS J212954-5620.1 A	0.833±0.017	0.845±0.012	4750±150	19
ASAS J212954-5620.1 B	0.703±0.013	0.718±0.017	4220±180	19
MG1-78457 A	0.527±0.002	0.505±0.008	3330±60	20
MG1-78457 B	0.491±0.001	0.471±0.009	3270±60	20
MG1-116309 A	0.567±0.002	0.552±0.013	3920±80	20
MG1-116309 B	0.532±0.002	0.532±0.008	3810±80	20
MG1-506664 A	0.584±0.002	0.560±0.004	3730±90	20
MG1-506664 B	0.544±0.002	0.513±0.008	3610±90	20
MG1-646680 A	0.499±0.002	0.457±0.006	3730±20	20
MG1-646680 B	0.443±0.002	0.427±0.006	3630±20	20
MG1-1819499 A	0.557±0.001	0.569±0.023	3690±80	20
MG1-1819499 B	0.535±0.001	0.500±0.014	3610±80	20
MG1-2056316 A	0.469±0.002	0.441±0.002	3460±180	20
MG1-2056316 B	0.382±0.001	0.374±0.002	3320±180	20
AK For A	0.6958±0.0010	0.687±0.020	4690±100	21
AK For B	0.6355±0.0007	0.609±0.016	4390±150	21
1SWASP J011351.29+314909.7 A	0.945±0.045	1.378±0.058	5961±54	22

1SWASP J011351.29+314909.7 B	0.186±0.010	0.209±0.011	3922±42	22
T-Cyg1-12664 A	0.680±0.021	0.613±0.007	4320±100	23
T-Cyg1-12664 B	0.341±0.012	0.897±0.012	2750±65	23
T-Cyg1-12664 A	0.680±0.045	0.799±0.017	5560±160	24
T-Cyg1-12664 B	0.376±0.017	0.3475±0.0081	3460±210	24

References. (1) Torres & Ribas (2002); (2) Ribas (2003); (3) López-Morales & Ribas (2005); (4) Morales et al. (2009a); (5) Morales et al. (2009b); (6) Bayless & Orosz (2006); (7) Devor et al. (2008b); (8) Irwin et al. (2011); (9) Irwin et al. (2009); (10) Clausen et al. (2009); (11) Çakırlı (2013); (12) Rożyczka et al. (2009); (13) Brogna (2006); (14) Birkby et al. (2012); (15) Carter et al. (2011); (16) Vaccaro et al. (2007); (17) Helminiak et al. (2012); (18) Helminiak & Konacki (2011); (19) Helminiak et al. (2011); (20) Kraus et al. (2011); (21) Helminiak et al. (2014); (22) Gómez Maqueo Chew et al. (2014); (23) Çakırlı et al. (2013); (24) this work.